Characterization of piezoelectric ZnO thin films and the fabrication of piezoelectric micro-cantilevers

by

Raegan Lynn Johnson

A thesis submitted to the graduate faculty
in partial fulfillment of the requirements for the degree of
MASTER OF SCIENCE

Major: Electrical Engineering

Program of Study Committee:
Robert J. Weber and Murti V. Salapaka, Co-major Professor
Co-major Professor

Iowa State University
Ames, Iowa
2005

David P. Cann

Graduate College
Iowa State University

This is to certify that the master's thesis of

Raegan Lynn Johnson

has met the thesis requirements of Iowa State University

Co-major Professor

Co-major Professor

For the Major Program

TABLE OF CONTENTS

List of Tables

List of Figures

Abstract

In Atomic Force Microscopy (AFM), a microcantilever is raster scanned across the surface of a sample in order to obtain a topographical image of the sample's surface. In a traditional, optical AFM, the sample rests on a bulk piezoelectric tube and a control loop is used to control the tip-sample separation by actuating the piezo-tube. This method has several disadvantages – the most noticeable one being that response time of the piezo-tube is rather long which leads to slow imaging speeds. One possible solution aimed at improving the speed of imaging is to incorporate a thin piezoelectric film on top of the cantilever beam. This design not only improves the speed of imaging because the piezoelectric film replaces the piezo-tube as an actuator, but the film can also act as a sensor. In addition, the piezoelectric film can excite the cantilever beam near its resonance frequency. This project aims to fabricate piezoelectric microcantilevers for use in the AFM. Prior to fabricating the cantilevers and also part of this project, a systematic study was performed to examine the effects of deposition conditions on the quality of piezoelectric ZnO thin films deposited by RF sputtering. These results will be presented. The deposition parameters that produced the highest quality ZnO film were used in the fabrication of the piezoelectric cantilevers. Unfortunately, the fabricated cantilevers warped due to the intrinsic stress of the ZnO film and were therefore not usable in the AFM. The complete fabrication process will be detailed, the results will be discussed and reasons for the warping will be examined.

Statement of Purpose

The purpose of this research project was to introduce and establish a process for fabricating peizoelectric MEMS micro-cantilevers for use in atomic force microscopes (AFM). Before attempting to fabricate the peizoelectric cantilevers, two things needed to happen. First, a process for bulk micromachining simple cantilevers needed to be determined. This was accomplished and the results will be presented. Second, a method for depositing and characterizing good quality piezoelectric zinc oxide films was required. The deposition of piezoelectric zinc oxide thin films using an RF sputter system marked the first time this particular system was used for piezoelectric films at Iowa State University. Films grown with different deposition parameters were compared and the parameters that produced the highest quality piezoelectric activity were used during the fabrication of the piezoelectric cantilevers. The fabrication of piezoelectric microcantilevers also marks the first time this has been attempted and accomplished at Iowa State University. Unfortunately, due to intrinsic stress in the ZnO films, the fabricated peizoelectric cantilevers ended up warping. The warping was significant enough that we were not able to test the cantilevers in the AFM. However, finite element analysis modeling was conducted to get an idea of how the cantilevers should respond to an applied voltage and to get an estimate of the cantilever sensitivity.

CHAPTER 1. Introduction

1.1 Atomic Force Microscopy

As the demand for smaller and faster products increases, characterization methods that are faster and more precise must also improve. Atomic force microscopy (AFM) is commonly used to characterize surface topography of given samples. Technologies affecting the electronics, biological, chemical, and automotive industries use the AFM to solve processing and materials problems. The materials being investigated include thin and thick film coatings, semiconductors, ceramics, metals, micromechanical properties of biological samples, nucleic acids, DNA and RNA, polymers and biomaterials, to name a few.

The AFM has made it possible to obtain 3-dimensional images of surfaces down to the atomic scale as well as measure forces on a nano-newton scale. The working components of the AFM are continually evolving. Work in this thesis will focus on one such area that will potentially improve the speed and preciseness of imaging surfaces of samples.

1.1.1 AFM background

Atomic Force Microscopy (AFM) was invented in 1986 by Binning, Quate and Gerber (1). Today, most AFMs use a laser beam deflection system which is shown schematically in Figure 1.1. In this optical AFM, a laser beam is reflected from the back surface of a cantilever beam onto a position-sensitive photodiode. The photodiode is divided into four quadrants. When the canatilever is not interacting with the sample, the laser is positioned at the center of the photodiode as a reference point. When the sharp tip of the cantilever beam comes in close contact with the sample, the cantilever beam bends in response to the forces between the tip and the sample which causes the laser beam to shift its position on the photodiode. As a

result, one quadrant of the photodiode will be illuminated more than another. By measuring the difference in light intensities between the upper and lower portions of the photodiode, a differential signal (A-B) is created and converted to a voltage signal. This signal is used in a control feedback loop to help maintain a constant force between the tip and the sample as the beam is raster scanned across the sample surface.

The sample typically sits on a positioning device made from piezoelectric ceramics. This positioning device, usually a tube scanner, is capable of sub-angstrom resolution in the x-, y-, and z-directions. Motion in the x- and y-directions typically performs the raster movement. Surface mapping is usually accomplished by maintaining a constant force between the tip and sample by moving the sample up and down with the help of a computer controlled feedback system. When the tip passes over a bump in the surface, the tip-sample separation becomes smaller which causes the cantilever to "feel" a force thereby bending the cantilever upward. The photodiode detects the deflection, converts the deflection to a voltage signal and adjusts the tip-sample separation by sending the signal to the z-piezo via the feedback system until the cantilever no longer experiences a deflecting force. The voltages used to maintain constant tip-sample forces are converted to distances and used to obtain the 3-dimensional image.

1.1.1.1 Force Curve

The radius of curvature of the very end of the cantilever tip can be on the order of 10 nm. The very sharp tip means that only a few atoms are involved in the tip-sample interaction and the forces between the tip and sample are governed by the intermolecular force curve shown in Figure 1.2. At the right side of the curve, the tip and sample are separated by a large distance and no force is experienced. As the atoms between the tip and sample are brought together, they first weakly attract each other. This attraction increases until the atoms are so close together that their electron clouds interact and begin to repel each other. The repulsive force continually weakens the attractive force as the distance decreases. When the distance between the atoms is a few angstroms, the force goes to zero. As the force becomes positive, the atoms between the tip and the sample come into contact with each other. The interaction between

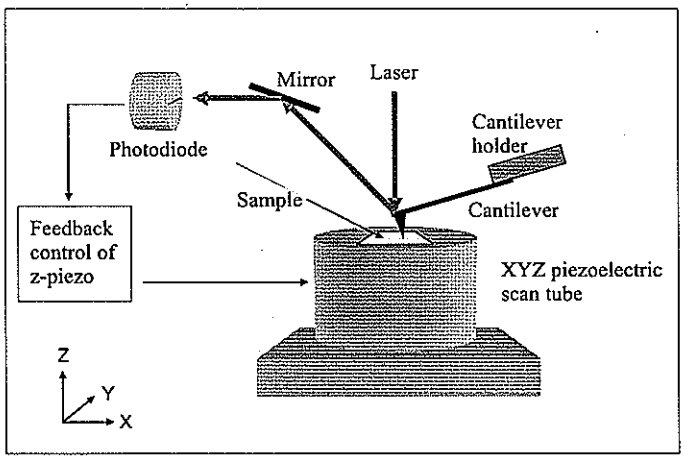

Figure 1.1 A simplified diagram of a traditional atomic force microscope (AFM).

the tip and the sample is important when talking about the different modes of operation.

1.1.1.2 AFM modes of operation

There are three commonly used modes of operation in the AFM: contact mode, non-contact mode and tapping mode.

Contact Mode In contact mode operation, as the name implies, the tip is in close contact with the sample surface as it is scanned over the sample. The force on the tip is in the repulsive regime of the inter-molecular force curve. By operating in the repulsive regime, high resolution images are obtained because the forces in this region are greater than in the attractive region. The main drawback to the contact mode of operation is that large lateral forces exist on the sample as the tip is dragged across the surface. Damage to the tip as well as the sample is possible.

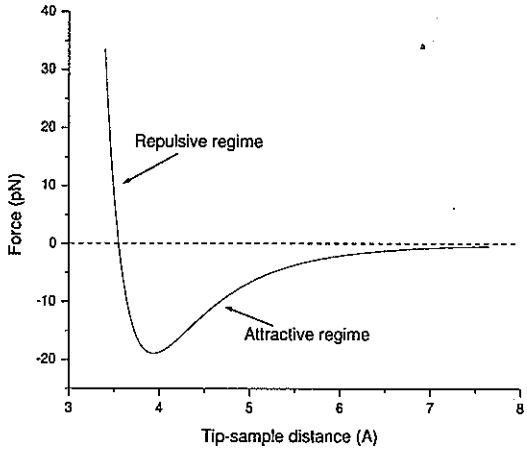

Figure 1.2 Intermolecular force curve.

Non-Contact Mode In non-contact mode operation, the tip of the cantilever hovers 50-150 $\AA$ above the sample surface. Attractive forces are the dominant forces between the tip and the sample. Forces in the attractive region are significantly weaker than forces in the repulsive region and, therefore, small oscillations are given to the tip of the cantilever via a dither piezoelectric crystal located within the cantilever holder. The forces between the tip and the sample are detected by measuring changes in amplitude, phase or frequency of the oscillating cantilever.

Tapping Mode In tapping mode operation, the tip of the cantilever is oscillated at or near the cantilever's resonant frequency and "taps" the surface of the sample. The tip of the cantilever comes into contact with the sample surface for very brief periods of time. By operating in the repulsive regime, high resolution is obtained, yet, the short duration of time that the cantilever is in contact with the sample limits the amount of damage associated with contact mode. The cantilever is driven at or near its resonant frequency by a dither piezoelectric crystal located within the cantilever holder. During scanning, the tip of the cantilever typically oscillates at a frequency of 50-500 kHz. As the tip comes in intermittent

contact with the sa e the a it e o osci ation is e ce e to ene oss he e ction in osci ation a it e is se to i enti an eas e s ace eat es

1.2 Piezoelectric Cantilevers

One common limitation of the AFM is the amount of time required to image surfaces on the micrometer scale. Typically the tip is scanned over an area at a rate of less than a few hundred microns per second. As a result, it often takes minutes to produce a single image (2). The reason for the slow scan speed is that the z-direction actuator is a bulk piezoelectric tube which has a relatively slow response time due to its large size. In a world where the demand for better and faster is never ending, the push for high-speed AFM imaging is in full force. One direction researchers are pursuing is to integrate a thin piezoelectric film onto the cantilever such that the beam will act as the z-direction actuator rather than using the bulky piezo-tube. Such a cantilever is called a piezoelectric cantilever.

Piezoelectric cantilevers have several advantages over conventional basic cantilevers, the first has already been mentioned. Another area where the AFM could use improvement is with the optical detection system. In optical AFM the laser has to be aligned on the back surface of the cantilever. This is a somewhat tedious and time consuming task to perform. Additionally, using an optical AFM to image in liquid environments is difficult as the laser light will reflect or refract at the air/water interface. Another disadvatantage of the optical AFM is that it allows for only one cantilever per laser beam, which, in a world where imaging with arrays of cantilevers is becoming more popular, presents a problem. One solution to these problems is to use a piezoelectric cantilever to detect or sense beam deflection rather than use optical detection.

Piezoelectric cantilevers can operate in three different modes: the beam can act as an actuator, the beam can act as a sensor, or the beam can self-oscillate. When used as an actuator, the piezoelectric cantilever has over 10 times the bandwidth of the piezo-tube which translates to increased imaging speed (2) and (3). When used as a sensor, the sensitivity of the system was as much as an order of magnitude better than that of the optical sensing method

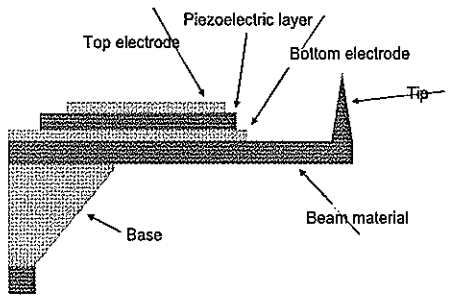

Figure 1.3 Cross sectional view of a typical piezoelectric cantilever.

(4). In self-oscillation mode, no external dither piezo was needed for the AFM in tapping mode.

The process for fabricating piezoelectric cantilevers has been documented in literature (5)-(7). Two piezoelectric films, PZT and ZnO, are commonly used for microcantilever applications. PZT has better peizoelectric response than ZnO, however, ZnO is easier to deposit and is more compatible with semiconductor and MEMS fabrication techniques. Although the fabrication steps may vary from group to group in the details, the same basic design is used. Namely, the piezoelectric layer is sandwiched between two electrodes and the whole package rests on top of a cantilever beam. A schematic of the cross section of a typical piezoelectric cantilever is shown in Figure 1.3.

When fabricating piezoelectric cantilevers, the beam material can be silicon, doped silicon, silicon nitride, silicon dioxide, or diamond. Electrodes are typically made from aluminum, gold, gold and chromium, gold and titanium, or chromium. The piezoelectric materials of choice are PZT and ZnO. The goal of this research project was to develop our own process and fabricate piezoelectric microcantilevers here at Iowa State University.

1.3 Thesis Organization

This thesis is divided into five remaining chapters. In Chapter 2, the theory of piezoelectricity will be discussed and the material properties of piezoelectric ZnO will be examined. Since the process of depositing piezoelectric ZnO was not a standard procedure at ISU prior to this project, a systematic study investigating ZnO film quality as a function of deposition parameters was required. Therefore, Chapter 2 will also detail the ZnO deposition process and measurement methods to characterize the quality of ZnO thin films and the results will be reported. Chapter 3 will outline the process used to fabricate a basic silicon nitride cantilever. Chapter 4 will pull Chapter 2 and Chapter 3 together by describing the process used to fabricate piezoelectric cantilevers. Chapter 5 will discuss the results of the basic cantilever and the results of the piezoelectric cantilever and Chapter 6 will provide a project summary and a discussion regarding future work.

CHAPTER 2. Piezoelectric Zinc Oxide

The degree of functionality of piezoelectric cantilevers strongly depends on the quality of the piezoelectric film. This chapter will first briefly discuss the theory of piezoelectricity and why ZnO was chosen as the piezoelectric material for this project. Then, since Iowa State University did not have a current process for depositing piezoelectric ZnO, the method for depositing ZnO will be introduced and the measurement techniques characterizing physical properties of ZnO films will be discussed. Finally, results for several ZnO films grown with different deposition parameters will be examined.

2.1 Theory of Piezoelectricity

In 1880, Pierre Curie and his brother Paul-Jaques discovered that an external force applied to certain crystals can generate a charge on the surface of the crystal found to be roughly proportional to the applied mechanical stress (8). One year later, they discovered the opposite also holds true; an applied voltage generates a deformation of the crystal. This interaction between electrical and mechanical systems is termed "piezoelectricity". The prefix "piezo-" is derived from the Greek word "press". The direct piezoelectric effect refers to the generation of an electric polarization due to a mechanical stress. Conversely, the indirect piezoelectric effect refers to the generation of a strain in a material due to the application of an electric field.

A simplified model of piezoelectricity involves the concept of anions ($-$) and cations ($+$) moving in opposite directions under the influence of an electric field or mechanical force. The forces generated by this motion cause lattice deformations for ionic crystals lacking a center of symmetry. Figure 2.1 shows what happens when a piezoelectric crystal is deformed. As a mechanical deformation (stress) is applied to the crystal, electric dipoles are generated due to

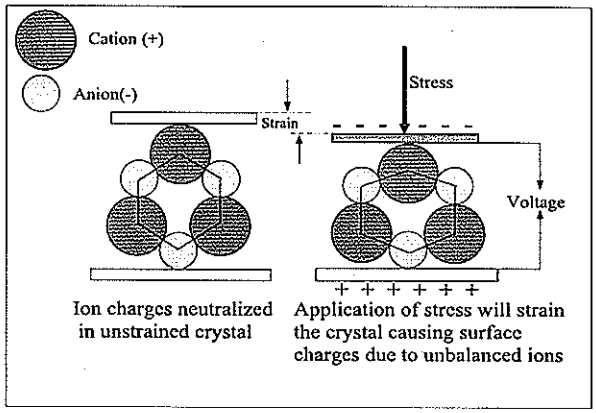

Figure 2.1 Piezoelectricity in an ionic crystal

the shifting of anions and cations and a potential difference develops. It should be noted that the potential difference in piezoelectric materials is a function of the *changing* stress; therefore, piezoelectric materials are typically used in dynamic situations.

2.1.1 Piezoelectricity in one-dimension

When an external stress is applied to a material, distortions or strains of the medium will result. Stress does not cause strain, nor does strain cause stress, but the two are coupled to each other and can be given by the following equation which is recognized as Hooke's Law,

$$\varepsilon = S\sigma \tag{2.1}$$

For this one-dimensional equation, ε represents the strain which is dimensionless, S is the elastic compliance coefficient (1/Pa), and σ is the stress (N/m^2). The compliance coefficient S relates the deformation produced to the application of the stress where $1/S$ = Young's modulus. Alternatively, Equation 2.1 can be written

$$\sigma = c\varepsilon \tag{2.2}$$

where c is the elastic stiffness constant or Young's modulus. Here, $c = 1/S$.

When a potential difference is applied across a dielectric material, an electric field is established which lines up the molecular dipoles and results in a polarization of the material $P = Np$, where P is the polarization (C/m^2), N is the number of dipoles per unit volume (m^{-3}) and p is the dipole moment (C·m). The polarization is proportional to the electric field,

$$P = \epsilon_0 \chi_0 E \tag{2.3}$$

where ϵ_0 is the permittivity of free space (F/m), χ_0 is the electric susceptibility (dimensionless), and E is the electric field (V/m). It is often easier to think in terms of electrical displacement,

$$D = \epsilon E = \epsilon_0 E(1 + \chi_e) = \epsilon_0 E + P \tag{2.4}$$

where D is the electrical displacement (C/m^2) and ϵ is the permittivity of the material (the relative permittivity ϵ_r is given by ϵ/ϵ_0).

Equations 2.1 and 2.2 contain only mechanical properties while Equation 2.3 and 2.4 contain only electrical properties. The Curie brothers demonstrated that electrical charges were produced when a pressure was applied to a piezoelectric material and that the surface charge density was proportional to the applied pressure. The following equation represents this phenomenon and links or couples the mechanical properties with the electrical properties of Equations 2.1-2.4. Electric polarization due to mechanical deformation is known as the direct piezoelectric effect and is given by

$$P_p = d\sigma \tag{2.5}$$

where d is the piezoelectric strain coefficient (C/N). The subscript p indicates that the polarization is a result of the piezoelectric effect and not as a result of an externally applied electric field.

The Curie brothers also demonstrated the reverse effect; namely, the strain resulting from the application of a potential difference across a piezoelectric material is proportional to the magnitude of the applied electric field. This effect, known as the indirect piezoelectric effect, is given by

$$\varepsilon_p = dE \tag{2.6}$$

Material	Coupling coefficient (k)
Quartz	0.1
AlN	0.24
ZnO	0.33
PZT	0.69

Table 2.1 Coupling coefficient of various piezoelectric materials (8).

Equations 2.5 and 2.6 state that the ratio between the resulting polarization and the magnitude of the applied stress (Equation 2.5) is equal to the ratio between the strain produced and the magnitude of the electric field (Equation 2.6, respectively).

The direct and indirect piezoelectric effects can be alternatively formulated by applying Equations 2.1 and 2.2,

$$P_p = d\sigma = dc\varepsilon = e\varepsilon$$

$$\sigma_p = c\varepsilon_p = cdE = eE$$

where e is the piezoelectric stress constant (C/m^2) and $e = dc$.

Another parameter critical to the phenomenon of piezoelectricity, especially when different piezoelectric materials are being compared, is the electromechanical coupling coefficient k. It is a measure of how much electrical energy is converted to mechanical energy (or vice versa). The coupling coefficient is defined as

$$k^2 = \frac{k_e^2}{1 + k_e^2} \tag{2.7}$$

where

$$k_e^2 = \frac{e_{33}^2}{c_{33}\epsilon_{33}} \tag{2.8}$$

The coupling coefficient for some common piezoelectric materials is listed in Table 2.1.

2.1.2 Tensor Notation

A more complex three-dimensional model is needed to describe real world piezoelectric phenomenon. When a physical stress is applied to a material in a particular direction, the

material will strain in not only the direction of the applied stress but in directions perpendicular to the stress as well. In other words, an x-direction stress couples to y- and z-direction strains; and the coupling is generally not the same for the different directions. Therefore, a three-dimensional model is needed.

The tensor notation used to describe the mechanical and electrical equations. Equations 2.1-2.4 can be written as follows; the mechanical equations become

$$\varepsilon_{ij} = S_{ijkl}\sigma_{kl} \tag{2.9}$$

$$\sigma_{ij} = c_{ijkl}\varepsilon_{kl} \tag{2.10}$$

and the electrical equation becomes

$$D_i = \epsilon_{ij}E_j \tag{2.11}$$

D_i and E_j are used in the electrical equation instead of the polarization P_i because they are more convenient and useful in practical analysis.

In these tensor equations, the indices i and j correspond to stress terms where $i = 1, 2, 3$ and $j = 1, 2, ...6$. The indices k and l correspond to strain terms where $k = 1, 2, 3$ and $l = 1, 2, 3$. It can be seen that when Hooke's law is applied to 3-dimensional geometry, it takes on a relatively complicated form because the stiffness coefficient couples two $3x3$ matrices which gives a total of 81 possible c or S terms.

Because of the symmetry of the strain and stress tensors the 81 terms of the coefficient matrix are reduced to 36 terms (for example $\varepsilon_{ij} = \varepsilon_{ji}$ and $\sigma_{kl} = \sigma_{lk}$ provided $i \neq j$ and $k \neq l$). Of these 36 terms, abbreviated subscripts can be used to make the equations easier to work with. When indices i and j are interchangeable, ij is abbreviated as λ ($ij \rightarrow \lambda$). The following convention for incides is used

$$11 \rightarrow 1,\ 22 \rightarrow 2,\ 33 \rightarrow 3,\ 23\ or\ 32 \rightarrow 4,\ 31\ or\ 13 \rightarrow 5,\ 12\ or\ 21 \rightarrow 6 \tag{2.12}$$

Similarly, when k and l are interchangeable, the indices kl are abbreviated to μ and follow the same pattern as seen in Equation 2.12.

It should be noted that an abbreviated component does not always stand for the corresponding tensor component. A multiplying factor is often needed depending on the value of

Stress	$\sigma_{ij} \rightarrow \sigma_\lambda$	
Strain	$\varepsilon_{ij} \rightarrow \varepsilon_\lambda$	$i = j$
	$2\varepsilon_{ij} \rightarrow \varepsilon_\lambda$	$i \neq j$
Elastic Stiffness	$c_{ijkl} \rightarrow c_{\lambda\mu}$	
Elastic Compliance	$S_{ijkl} \rightarrow S_{\lambda\mu}$	$i = j$ and $k = l$
	$2S_{ijkl} \rightarrow S_{\lambda\mu}$	$i \neq j$ or $k \neq l$
	$4S_{ijkl} \rightarrow S_{\lambda\mu}$	$i \neq j$ and $k \neq l$

Table 2.2 Abbreviated indices compared to their respective tensors.

i, j, j and k. For instance, shear strain ε_4, ε_5 or ε_6 is not the respective component of tensor strain ε_{23}, ε_{31} or ε_{21}, but is equal to twice the latter. Table 2.2 shows how the abbreviated indices are related to the respective tensor component by a multiplicative factor.

Using the abbreviated tensor notation Equations 2.9 and 2.10 can be written as

$$\varepsilon_\lambda = S_{\lambda\mu}\sigma_\mu \tag{2.13}$$

$$\sigma_\lambda = c_{\lambda\mu}\varepsilon_\mu \tag{2.14}$$

where $\mu = 1, 2, ...6$.

The direct piezoelectric effect in three dimensions can then be expressed as,

$$P_i = d_{i\mu}\sigma_\mu \tag{2.15}$$

while the indirect effect can be expressed as

$$\varepsilon_\mu = d^t_{i\mu}E_i \tag{2.16}$$

(here, d^t is the transpose of the piezoelectric strain matrix).

In these equations, $i = 1, 2$, and 3 make up the indices of the components of polarization and $\mu = 1, 2, ...6$ the indices of the components of mechanical stress and strain. For example, for the piezoelectric constant, d, the first subscript i refers to the direction of the field where the subscripts 1, 2, and 3 indicate the x, y, and z directions, respectively. The second subscript μ refers to the direction of the tensile or shear stress. Of the stress tensor's six components, $\mu = 1, 2$, and 3 represent compression or tensile stresses while $\mu = 4, 5$, and 6 represent shear

$\epsilon_{ij} \Rightarrow 3x3$ matrix
$d_{i\mu} \Rightarrow 3x6$ matrix
$e_{i\mu} \Rightarrow 3x6$ matrix
$c_{\lambda\mu} \Rightarrow 6x6$ matrix
$S_{\lambda\mu} \Rightarrow 6x6$ matrix

Table 2.3 Piezoelectric constants and tensor dimensions.

stresses. As an example, $d_{i\mu} = d_{33}$ represents an electric field parallel to the z-axis and a piezoelectric-induced tensile strain in the z-direction.

Table 2.3 shows common constants used in solving piezoelectric problems and the respective dimension of each tensor.

2.2 Piezoelectric Zinc Oxide

As was mentioned earlier, one of the defining characteristics of a piezoelectric material is the lack of a center of symmetry in the unit cell. Figure 2.2 shows the crystal structure of zinc oxide. ZnO forms a hexagonal wurtzite structure with $6mm$ symmetry. It possesses the lack of center symmetry required for piezoelectric materials. The coupling coefficient for ZnO is also relatively high which makes ZnO an excellent material to use in a wide variety of piezoelectric applications.

Due to symmetry in the hexagonal ZnO crystal, the physical parameters and physical constants associated with ZnO can be reduced to the following matrices.

$$\epsilon_{\lambda\mu} = \begin{bmatrix} \epsilon_{11} & 0 & 0 \\ 0 & \epsilon_{11} & 0 \\ 0 & 0 & \epsilon_{33} \end{bmatrix} \tag{2.17}$$

$$d_{i\mu}, e_{i\mu} = \begin{bmatrix} 0 & 0 & 0 & 0 & d_{15} & 0 \\ 0 & 0 & 0 & d_{15} & 0 & 0 \\ d_{31} & d_{31} & d_{33} & 0 & 0 & 0 \end{bmatrix} \tag{2.18}$$

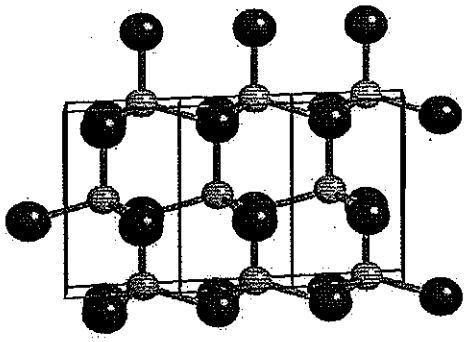

Figure 2.2 The Hexagonal wurtzite crystal Structure of ZnO. The larger red atoms are zinc atoms while the smaller purple atoms are oxygen atoms. (9)

$$c_{\lambda\mu}, S_{\lambda\mu} = \begin{bmatrix} c_{11} & c_{12} & c_{13} & 0 & 0 & 0 \\ c_{12} & c_{11} & c_{13} & 0 & 0 & 0 \\ c_{13} & c_{13} & c_{33} & 0 & 0 & 0 \\ 0 & 0 & 0 & c_{44} & 0 & 0 \\ 0 & 0 & 0 & 0 & c_{44} & 0 \\ 0 & 0 & 0 & 0 & 0 & c_{66} \end{bmatrix} \tag{2.19}$$

where $c_{66} = \frac{1}{2}(c_{11} - c_{12})$ and $S_{66} = 2(S_{11} - S_{22})$.

The values of each of the independent parameters are given in Table 2.4.

2.3 ZnO film growth and characterization methods

In addition to piezoelectric devices, ZnO is used in a variety of other scientific applications including acoustic wave devices, semiconductors, photoconductors, and optical waveguides (12). Therefore, many different deposition methods have been developed. ZnO films can be deposited by a variety of deposition techniques such as sol-gel process (13), spray pyrolysis (14), chemical vapor deposition (CVD) (15), molecular beam epitaxy (MBE) (16) and sputtering (17)-(20). Sputtering is the most commonly used deposition method because it is possible to

Parameter	Value	Units
ρ	5.675	$(10^3 kg/m^3)$
ϵ_{11}/ϵ_0	8.5	dimensionless
ϵ_{33}/ϵ_0	10.9	
d_{33}	12.4	$(10^{-12}C/N]$
d_{31}	-5.0	
d_{15}	-8.3	
e_{33}	1.57	(C/m^2)
e_{31}	-0.36	
e_{15}	-0.36	
c_{11}	210	$(10^9 N/m^2)$
c_{12}	121	
c_{13}	105	
c_{33}	211	
c_{44}	43	

Table 2.4 Physical constants of Piezoelectric ZnO (10), (11).

grow oriented films with uniform thickness on a wide variety of substrates. For this reason, sputtering was the deposition method of choice for this research project.

2.3.1 RF Magnetron Sputtering Overview

Sputter deposition is widely used in semiconductor and MEMS technology, and, as a result, is described in detail in literature. For an in-depth discussion regarding sputtering, see (21)-(22). What follows is a brief discussion on the principles underlying the technology. The sputtering process can be compared to throwing steel balls at a concrete wall. As the balls strike the wall, small fragments of concrete tear away from the wall. If the process is continued, eventually the surrounding area will be covered in a thin layer of concrete dust. In sputtering, the "steel balls" are ionized atoms while the "concrete wall" is a plate of the material to be sputtered (i.e. the target material).

Figure 2.3 shows a simplified RF magnetron sputter system. In a typical sputter system, an inert gas, such as argon, is fed into the sputter chamber which is at a low pressure. In DC sputtering, a voltage is applied across two parallel electrodes causing the argon to ionize

accelerating Ar^+ and e^- in opposite directions. Collisions between these charged particles and neutral Ar atoms cause further ionization thereby generating a plasma. The plasma contains neutral atoms, positive ions and free electrons. In a DC sputter system, the positive ions (the "steel balls") in the plasma are accelerated toward the negative electrode which is conductive target material (the "concrete wall"). The energetic ions strike the target and dislodge or sputter the target atoms. These atoms are then free to travel through the plasma as vapor and strike the surface of the substrate where they condense and form the deposited film. The sputtered atoms are free to land anywhere within the deposition chamber which means the location of the substrate with respect to the target is critical.

When an insulating target is desired, a high frequency alternating voltage is coupled capacitively through the target to the plasma so that conductive electrodes are not necessary. This is known as radio frequency or RF sputtering. The frequency is chosen to be high enough so that a continuous plasma discharge is maintained. The conventional frequency is at 13.56 MHz.

In both DC and RF sputtering, the efficiency of ionization from energetic collisions between the electrons and gas ions is rather low. In some situations, magnets are used to confine the electrons near the target. This increases the percentage of electrons that take part in ionization events which increases the ionization efficiency. The addition of a magnetic field is known as magnetron sputtering. Usually, a magnet is placed behind the target to create a magnetic field that is perpendicular to the electric field. The electrons are then trapped near the surface of the target and are forced in a spiral motion until they collide with an argon atom. The effective increase in electrons increases the amount of argon ions which ultimately increases the sputtering rate.

2.3.1.1 RF magnetron sputter system

ZnO films show the best piezoelectric activity when the c-axis of the crystal is oriented perpendicular to the surface of the substrate, ie. along the (002) direction (23) - (26). For depositing ZnO thin films using RF sputtering either a pure metallic Zn target or a high

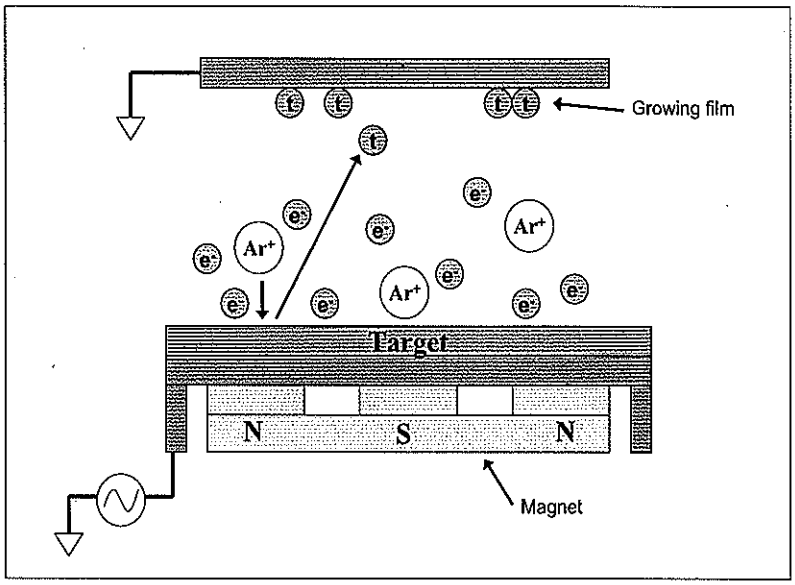

Figure 2.3 Simplified diagram of an RF magnetron sputter system. Electrons collide with gas atoms causing the atoms to ionize. These ionized atoms then bombard the target and dislodge target atoms which travel as vapor to the substrate or any other surface before condensing and forming a film.

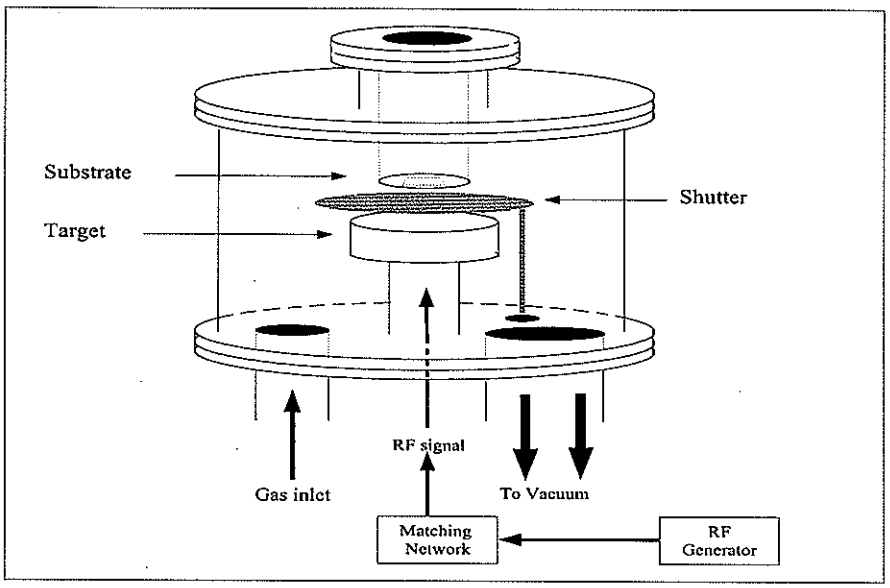

Figure 2.4 The RF magnetron sputter system at the MRC.

purity ZnO target can be used. Typically, a high purity mixture of argon and oxygen gas is used during deposition. The exact ratio of argon to oxygen is dependent on the target used and on each specific system. For example, a system using a Zn target will typically use oxygen concentrations of 80% to pure oxygen, whereas, a system using a ZnO target will use oxygen concentrations of 10-80%.

In this study, we used a home built RF magnetron sputter system which is shown schematically in Figure 2.4. In this system, the substrate was held firmly against the substrate holder by a stainless steel mask which had a 1.5 inch square opening. The substrate holder was loaded in from the top of the chamber so the substrate was parallel to the ground. The target was a Mighty Mak 3 inch 99.999% ZnO target that sat parallel to the substrate 2.54 cm below the loaded substrate holder. The substrate temperature was controlled by a temperature controller connected to a thermocouple mounted in a recess on the back of the substrate holder. A movable shutter separated the target and the substrate and was manually controlled from outside the chamber.

The target was bonded to a copper backing plate which was attached to the magnet. The magnet consisted of a circular core surrounded by an opposite poled outer ring. The target also sat atop a cooling block which had a continuous circulation of chilled water running through. The target needed water cooling as most of the energy deposited by the incident Ar atoms dissipates in the target as heat, which could lead to excessive heating.

A power feed rod connected a conductive plate to the 13.56 MHz RF source, located outside the camber. The RF power control and RF tuner were located outside the chamber. A matching network for the specified frequency was set up between the generator and the plasma chamber to ensure the best power transfer.

The gases used during deposition entered through a valve at the bottom of the chamber. Both an ultra high purity argon tank and an ultra high purity oxygen tank were used. The flow rates of the two gases were controlled by a mass flow controller with typical flow rates of 40 sccm for argon and 5-25 sccm for oxygen.

The deposition chamber was evacuated by a turbomolecular pump using Fomblin vacuum fluid designed specifically to handle high concentrations of oxygen. The turbo pump was backed by a mechanical backing pump. The mechanical roughing pump was used to initially evacuate the chamber to a pressure of 1 torr. During deposition, the pressure was controlled through a gate valve by the turbo pump.

2.3.1.2 ZnO film growth

This was the first time RF sputtered ZnO films had been deposited at Iowa State University (using this particular sputtering system). Before the piezoelectric cantilevers could be fabricated, deposition parameters that gave the highest quality piezoelectric ZnO thin films had to be determined. ZnO thin films were deposited for different oxygen concentrations, different substrate temperatures, different power levels and different chamber pressures. The growth rate of the films was determined by measuring the thickness of the film and the orientation of the crystals was determined by x-ray diffraction. To determine the piezoelectric activity, a resonator structure was fabricated and the frequency response was measured using a network

analyzer.

Since the piezocantilevers were to consist of a silicon nitride beam, a bottom aluminum electrode, a ZnO piezoelectric layer, and a top aluminum electrode, the calibration of the ZnO films was performed on a similar substrate – a silicon wafer coated with silicon nitride and aluminum. This was done to ensure comparable piezoelectric properties between the film used for characterization and the film on the cantilever beam as the quality of the ZnO film does depend on the underlying layer (20).

The substrate for the ZnO films was a 4 inch double sided polished (100) silicon wafer with approximately 2 μm of silicon nitride followed by 2000 $\AA$ of aluminum. The 4 inch wafer was cleaved in quarters to obtain a substrate size that was compatible with the substrate holder – a 3 inch diameter holder with a 1.5 inch square mask opening.

After loading the substrate into the sputter system, 10 nitrogen purges were performed to remove any moisture that may have entered the system during the brief time it was open to the atmosphere. While purging, the substrate temperature was ramped up to the desired set point. Once the chamber had pumped down to a pressure of $2x10^{-6}$ torr and the desired substrate temperature obtained, the gas valves were opened and the flow rates set to the proper value. The RF power was then turned on. The tuning was adjusted to minimize the reverse RF power. The opening of the gate valve was adjusted until the desired chamber pressure was obtained.

After the plasma was ignited and the desired parameters set, the target was conditioned for 3 minutes to remove any contaminants such as dust that may have fallen on the target (or to remove any oxidation that had occurred on the target surface). To ensure the substrate was not coated with this conditioning layer, the shutter between the target and the substrate was closed. After the target conditioning layer was complete, the shutter was opened to begin deposition. After the shutter was opened and the timer triggered, the deposition conditions were checked periodically to ensure consistency.

To grow 1 μm thick films, deposition times varied due to differences in growth rates which depended on deposition conditions. A typical growth rate was $\sim$ 1 μm/hr. The deposition

was stopped by first closing the shutter, then turning off the plasma by shutting off the RF power and last closing off the gas lines. After the substrate cooled to 80 °C, the chamber was brought to atmospheric pressure and the substrate was removed from the substrate holder.

2.3.2 ZnO Film Characterization

After the ZnO film was deposited, the quality of the film needed to be determined. First, the thickness of the film was measured in order to determine the growth rate. Then since films with good piezoelectric activity possess a strong c-axis crystal orientation, x-ray diffraction measurements were performed to determine the crystallographic orientation. Lastly, the piezoelectric activity of the film was determined by measuring the frequency response of a bulk acoustic wave resonator.

2.3.2.1 Thickness measurement

UV/VIS/NIR spectrophotometry was used to determine the thickness of the deposited ZnO films. The system used to determine the spectra was a split beam apparatus manufactured by Perkin-Elmer and which is interfaced to a PC. The split-beam spectrophotometer generated a single monochromatic light beam that was then split by optics into two parallel beams. One of the beams was aimed directly at the photo-dectector and was used as a reference. The other beam passed through an integrating sphere, was reflected off the film and substrate and then directed to the photo-detector. The difference between the two beam powers was measured by the photo-detector.

Light that was not reflected off the surface of the film was either transmitted through the film (and reflected off the surface of the aluminum) or absorbed. The light reflected off the film surface and the light reflected off the aluminum surface create an interference pattern, much like an oil slick on pavement. A reflection vs. wavelength spectra for a typical ZnO film is shown in Figure 2.5.

The interference can be used to determine the thickness of the film by comparing adjacent

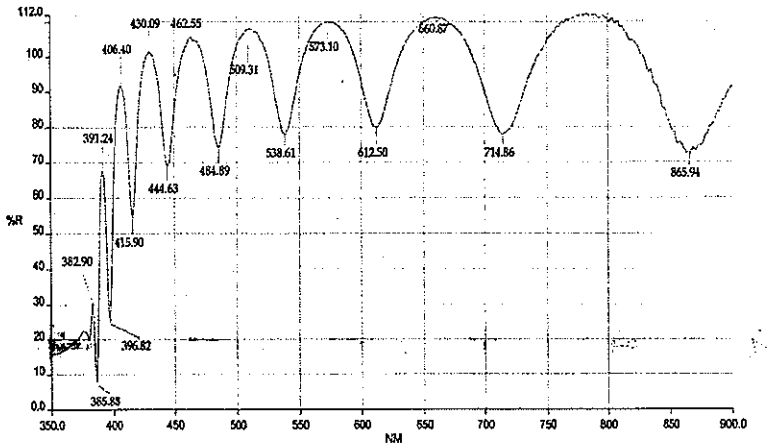

Figure 2.5 Typical reflection vs. wavelength spectra for a ZnO film.

λ	450 nm	288 nm	500 nm	515 nm	550 nm	600 nm	633 nm	1000 nm
n	2.106	2.064	2.051	2.044	2.025	1.999	1.990	1.944

Table 2.5 Refractive index of ZnO as a function of wavelength (28).

peaks or valleys (27), that is

$$t = \frac{i(\lambda_1 \lambda_2)}{2n(\lambda_2 - \lambda_1)}. \tag{2.20}$$

Here, t is the calculated film thickness, i is the number of complete cycles from λ_1 to λ_2, n is the refractive index of the film and λ_1 and λ_2 are the values of wavelengths at two maxima or two minima in the reflection plot.

The refractive index n for ZnO varies as a function of wavelength. A chart given in Table 2.5 (28) was used for this study with a typical index of refraction between 2.0 and 2.1 for the wavelengths we used.

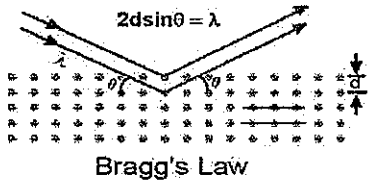

Figure 2.6 x-ray beams interacting with atoms in a periodic crystal. (29)

2.3.2.2 x-Ray Diffraction

x-Ray diffraction (XRD) is a common technique for determining the cyrstallographic structure of a material. For this project the XRD instrument used was a Seiman's x-ray diffractometer located in the Material Analysis Research Laboratory at Iowa State University.

XRD examines the scattering of x-rays from a sample after an incident x-ray interacts with electrons in atoms. The incoming x-rays collide with electrons causing elastic or inelastic scattering. No energy is lost in elastic collisions, therefore, the wavelength of the scattered x-rays is the same as the incident wavelength and only momentum has been transferred. These scattered x-rays carry information about the electron distribution in materials.

Diffracted waves from different planes of atoms will interfere with each other creating a diffraction pattern. Atoms that are arranged in a periodic fashion will yield a diffraction pattern with sharp interference maxima (peaks). The peaks in an x-ray diffraction pattern are related to the unit cell dimensions. The condition for a diffraction peak to occur can be found using Bragg's Law:

$$2d\sin\theta = n\lambda \tag{2.21}$$

Here, d is the distance between lattice planes, θ is the scattering angle, n is an integer representing the order of the diffraction peak, and λ is the wavelength of the x-ray. Figure 2.6 shows a 2D periodic crystal lattice with the incident and reflected x-rays.

The diffraction pattern is typically a plot of the scattering intensity vs. the scattering

Parameter	Standard Reference Value for ZnO
a=b	3.24982 Å
c	5.20661 Å
2θ	34.420^o
d-spacing	2.6033 Å

Table 2.6 Lattice parameters, 2θ and d-spacing of a standard ZnO reference. The 2θ and d-spacing values are for the (002) peak. (30)

angle 2θ. The peak positions, intensities, peak width and peak shape all provide important information about the structure of the material. A sharper peak with high scattering intensity indicates that a sample has good crystallinity. When obtaining the XRD scan for the ZnO films, a film with good orientation along the c-axis was desired. Therefore, a film showing sharp, intense (002) peaks should have a high probability of being piezoelectric. Table 2.6 shows important parameters of a standard reference ZnO powder.

The lattice parameters of a crystal can be calculated by knowing the d-spacing value which is determined from the peaks of the XRD scan. For a hexagonal system, the d-spacing is related to the lattice parameters by

$$\frac{1}{d^2} = \frac{4}{3}\left(\frac{h^2 + hk + k^2}{a^2}\right) + \frac{l^2}{c^2} \tag{2.22}$$

where h, k, and l are the Miller indices, and a, b and c are the lattice parameters along the x-, y-, and z-directions. Since we are primarily concerned with the (002) direction of ZnO, then $h = 0$, $k = 0$ and $l = 2$. Solving for c in Equation 2.22, we find

$$c = 2d \tag{2.23}$$

Figure 2.7 shows a typical XRD scan of the ZnO thin films grown for this project. The scan ran from 2θ=20^o - 53^o. For this particular scan, only the (002) is present. The strong (002) peak and the lack of any peaks with h or $k \neq 0$ indicates good orientation. For a (002) peak, position 2θ=34.443^o, d=2.6017 $\AA$, and, from Equation 2.23, we obtain c=5.2034 $\AA$. The theoretical value (Table 2.6) is 5.20661 $\AA$. The difference between the theoretical and actual lattice dimensions can be attributed to strain in the material.

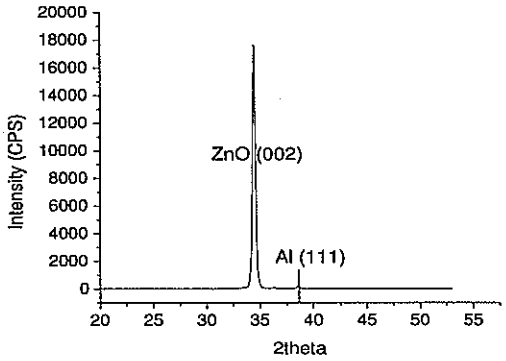

Figure 2.7 An example of an ZnO XRD scan.

2.3.2.3 ZnO resonators

The test structure used to determine the piezoelectric activity of ZnO was a bulk acoustic wave microstrip resonator. The RF measurement used for testing the resonators is a standard method for small microwave devices referred to as microstrip probing. Frequency measurements for microwave device often use the Smith Chart which is shown in Figure 2.8. The Smith chart is a polar plot of the complex reflection coefficient Γ, also known as the scattering parameter s. The reflection coefficient Γ_L is defined as the ratio between the reflected voltage wave V_{refl} and the incident voltage wave V_{inc}, that is,

$$\Gamma_L = \frac{V_{refl}}{V_{inc}} = \frac{Z - Z_0}{Z + Z_0} = \Gamma_r + j\Gamma_i \tag{2.24}$$

Here, Z is the load impedance and Z_0 is the characteristic impedance. Note that $Z = R + jX$ where R is the real part of the impedance or resistance and X is the imaginary part of the impedance or the reactance. The Smith chart maps the right half of the impedance plane (of the real vs. imaginary impedance values) inside a unit circle. Using the unit circle allows one to view resistance or reactance values from zero to infinity at a glance.

The Smith chart was used to analyze the piezoelectricity of the ZnO films. The bulk acoustic wave microstrip resonator consists of a ZnO film that was deposited atop the aluminum, silicon

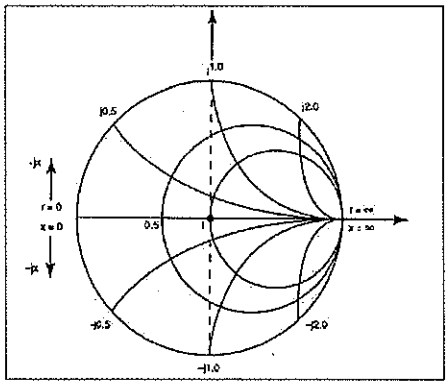

Figure 2.8 A simple representation of a Smith chart (31).

nitride, silicon substrate. An aluminum layer was deposited and patterned on top of the ZnO to act as the top conductor of the bulk acoustic wave device. The pattern of this top conductor is shown in Figure 2.9. A three-dimensional illustration of the resonator is shown in Figure 2.10.

The devices were characterized by a standard method for measuring small microwave devices referred to as microstrip probing. The probe heads used had a uniform center-to-center spacing of 100 mils at the end of a coaxial high frequency feed line. The probe was a ground-signal-ground probe where the "signal" probe head rested on the contact pad extending from the resonator bar and the two "ground" probes rested on the contact pads situated on either side of the signal contact pad. The test set-up used is shown in Figure 2.11. The frequency signal was applied to the test structure and the s_{11} reflection coefficient was measured.

Figure 2.12 shows a typical piezoelectric response on the Smith chart of a ZnO film. Figure 2.12a shows the resonator response for a frequency range of 3 MHz - 6 GHz. The plot of the s parameter looks similar to a capacitor and resistor in series with the exception of the resonance loop. Figure 2.12b shows the response of the same resonator at its resonance frequency. The diameter of the circle is related to the amount of piezoelectric activity of the film. The location of the circle depends on the frequency at which the resonator resonates which depends on the film thickness as well as depends on the rate at which the frequency is swept.

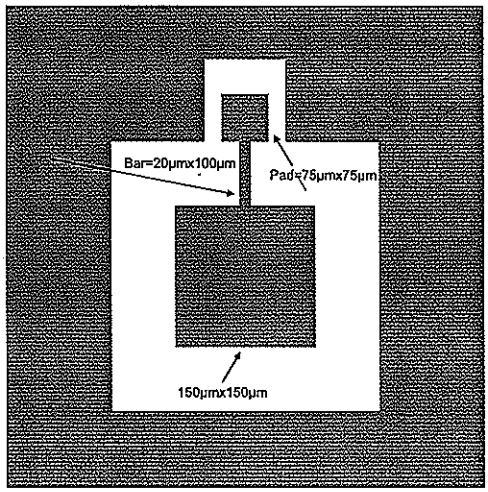

Figure 2.9 Resonator mask design. The signal probe will make measurements at the top pad while the ground probes rest on the large metal areas on either side of the pad.

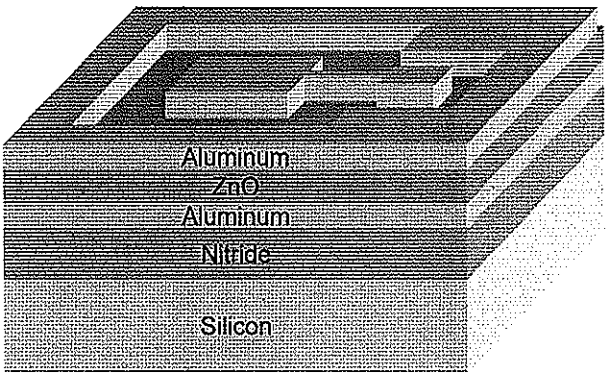

Figure 2.10 3D structure of bulk acoustic wave resonator used to test the piezoelectricity of the ZnO film.

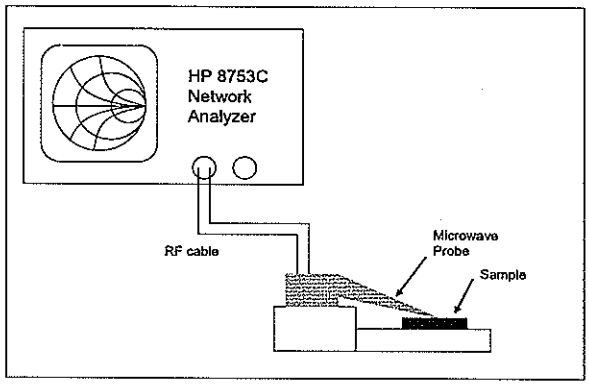

Figure 2.11 Microwave probing of the bulk acoustic wave resonator structure.

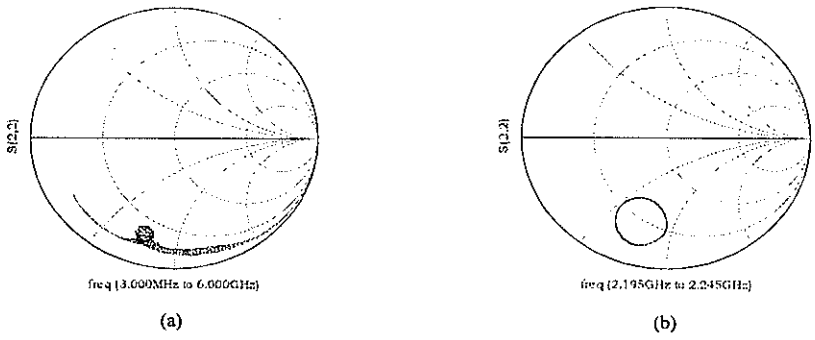

Figure 2.12 A typical plot showing the amount of piezoelectric activity of a ZnO bulk acoustic wave resonator (a) for the frequency range 3 MHz - 6 GHz and (b) at resonance of 2.2 GHz.

2.3.3 ZnO Results

The quality of the ZnO film is critical when it comes to using the ZnO film in a piezoelectric device. There is a strong correlation between the degree of c-axis orientation and the amount of piezoelectric activity. Therefore, films with high c-axis orientation are desired. This project marked the first time the home-built sputter system at the MRC was used to produce ZnO thin films. For this reason, a systematic study examining film quality as a function of deposition conditions was required. Numerous films were grown for various oxygen concentrations, various temperatures, various RF power levels, and various chamber pressures during deposition and the quality of the film was determined by x-ray diffraction (XRD) and by the results of the bulk acoustic wave resonators.

The target-to-substrate distance was fixed for all films at 2.54 cm. All films were grown on 2000 $\AA$ of aluminum which was on approximately 2 μm of silicon nitride that had been deposited on a (100) n-type silicon wafer. The ZnO deposition procedure was outlined in Section 2.3.1.2.

2.3.3.1 Oxygen Concentration

Several other research groups (32)-(34) have found that extra oxygen is needed in the deposition chamber during deposition. The presence of extra oxygen is to compensate for the depletion of oxygen in the ZnO film. The ZnO molecule will dissociate after leaving the target material thus creating free Zn and free oxygen atoms. Occasionally the free Zn atoms will not recombine with oxygen before reaching and incorporating into the substrate thus causing excess zinc in the film.

We studied the effects of four different argon-to-oxygen gas ratios. The ratios consisted of 20%, 30%, 50%, and 70% percent oxygen in the chamber. It should be noted that the gas ratios are calculated as a function of total number of atoms in the chamber. O_2 gas consists of two oxygen atoms. An oxygen gas flow rate equal to half the Ar flow rate means the chamber consists of 50% oxygen atoms and 50% argon atoms. The remaining deposition parameters were identical for each of the films. The temperature was set to 150 °C, the chamber pressure

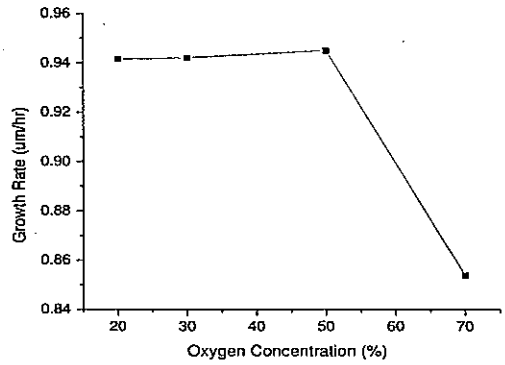

Figure 2.13 ZnO growth rate as a function of oxygen concentration.

was 10 mtorr, and the RF power was 75 Watts.

The growth rate as a function of oxygen concentration is shown in Figure 2.13. The growth rate dramatically decreases at the highest oxygen concentration presumably because the extra oxygen molecules are actually etching away parts of the film thus decreasing the growth rate.

Figure 2.14 shows the XRD spectra for the series of films grown with differing oxygen concentrations. All of the films show good (002) orientation, though the film grown with 50% oxygen shows the highest intensity peak implying that this film may have better orientation than other films.

These XRD results, suggest that the film with the best (002) orientation was deposited in the presence of 50% oxygen. The piezoelectric activity (Figure 2.15) confirms the fact that the film grown with 50% oxygen gave the most favorable results as the resonance circle was the largest for this particular film.

2.3.3.2 Substrate Temperature

The substrate temperature plays an important role in the quality of the ZnO film (32) and (35). These groups have found that the orientation of the film is better for for films grown with substrate temperatures of 150 ^{o}C or lower, possibly because higher temperatures cause re-

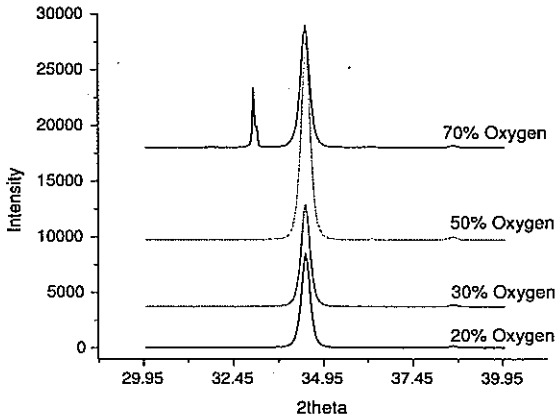

Figure 2.14 XRD scan of ZnO films deposited at different oxygen concentrations.

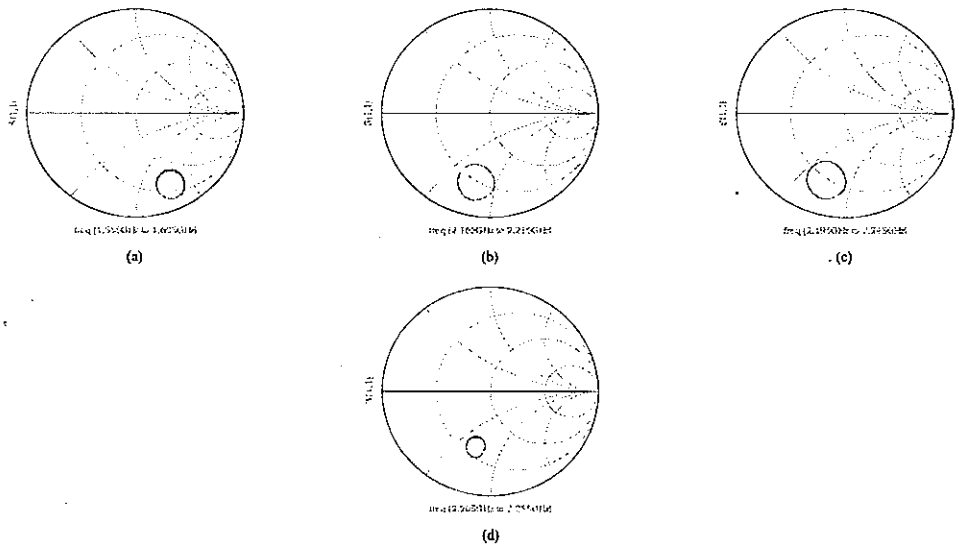

Figure 2.15 Resonator results for various oxygen concentrations – (a) 20%, (b) 30%, (c) 50% and (d) 70%.

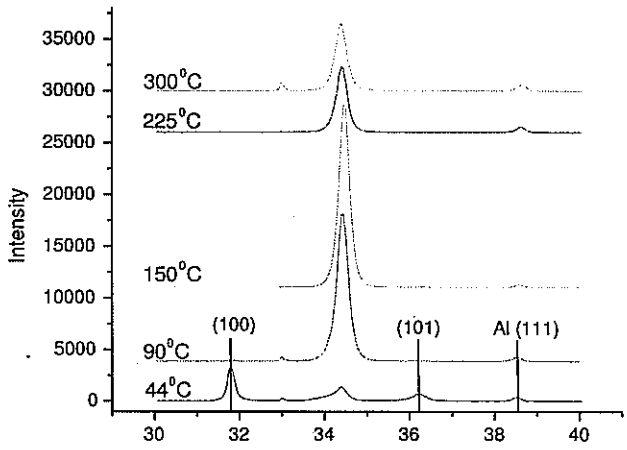

Figure 2.16 XRD scan of ZnO films grown at different substrate temperatures.

sputtering of the deposited film. For the temperature comparison study, the other deposition parameters were fixed at 50% oxygen concentration, 10 mtorr pressure and 75 Watts RF power. The substrate temperatures ranged from 44 °C to 300 °C.

Figure 2.16 shows the XRD results for the five different deposition temperatures that were studied. At a deposition temperature of 44 °C, the film did not show the preferred (002) direction. As the deposition temperature increased, the intensity of the (002) peak also increased while the (100) peak disappeared all together. At 300 °C, the film had (002) orientation, but the intensity of the peak was rather weak. From these XRD spectra, the film grow with a substrate temperature of 150 °C was the best.

The s_{11} parameters of the resonators grown with different substrate temperatures are shown in Figure 2.17. The low deposition temperature did not produce a very high quality ZnO film based on the results of the piezoelectric activity which is consistent with the results of the x-ray spectra. The film grown at 150 °C shows the largest circle on the Smith chart indicating that this film had the best piezoelectricity. From the XRD and resonator results, it is clear

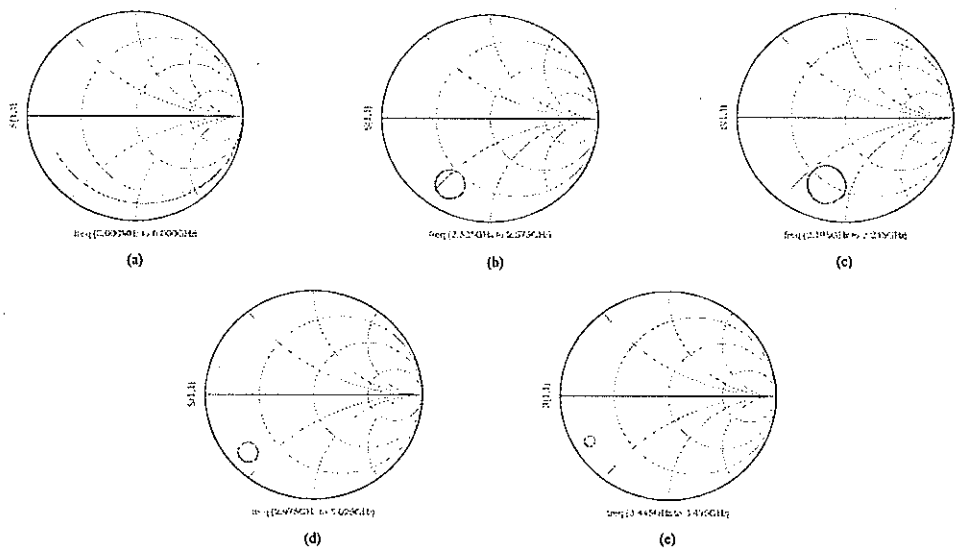

Figure 2.17 Piezoelectric activity of ZnO films with deposition temperatures of (a) 44 °C, (b) 90 °C, (c) 150 °C, (d) 225 °C and (e) 300 °C. No activity was observed for the film deposited at 44 °C – a capacitive-like result over the frequency range 3 MHz - 6 GHz is shown in Figure (a).

that the deposition temperature that produces the best quality ZnO film was 150 °C.

2.3.3.3 RF Power

The RF power is an important parameter to consider when depositing ZnO mostly because it heavily influences the growth rate of ZnO. Several other research groups (34), (36) suggest that the deposition rate should be kept at 1 μm/hr or lower to achieve high-quality ZnO films. Higher RF power levels not only increases the deposition rate but also increases the number of high-energy atoms, ions and electrons in the plasma thus increasing the probability of defects in the crystal.

In this study, the RF power ranged from 50 Watts to 250 Watts. All other parameters were held constant at 50% or 20% oxygen concentration, 150 °C deposition temperature and 10 mtorr chamber pressure. Figure 2.18 shows the nearly linear dependence of deposition rate

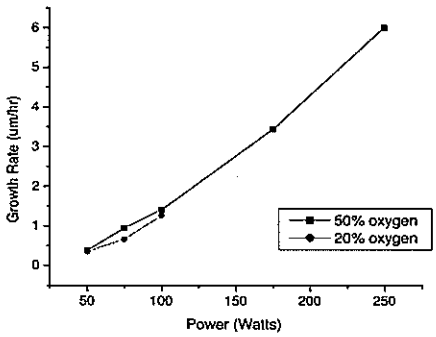

Figure 2.18 Deposition rate of ZnO as a function of RF power for films with 20% oxygen and 50% oxygen.

on RF power.

The XRD spectra of each RF power level are shown in Figure 2.19. Notice that the (100), (101) and (102) directions were more prevalent at higher power levels. Figure 2.20 shows the resonator results. As expected, the piezoelectricity was strongest for films with high (002) orientation, ie. the film deposited with RF power of 75 Watts.

2.3.3.4 Chamber Pressure

When studying the effects of chamber pressure during deposition the other deposition parameters were fixed at 50% oxygen concentration, 150 °C temperature and 75 Watts power. Park *et al.* (33) discovered that the deposition pressure influences the grain size and surface roughness more than any other deposition parameter. In our study, we did not focus on grain size, however, based on the x-ray spectra (Figure 2.21), the deposition pressure did have some influence on the crystallite structure. The orientation of crystallites in ZnO film was not dependent on deposition pressure, however, the number of (002) crystallites found in the film was highly dependent on deposition pressure. The strongest piezoelectric activity occured on the film grown with a chamber pressure of 10 mtorr as is seen in Figure 2.22.

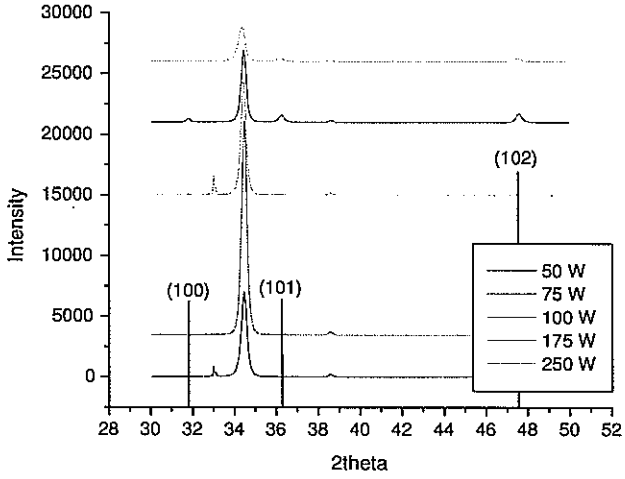

Figure 2.19 XRD scan of ZnO films deposited at different RF power levels.

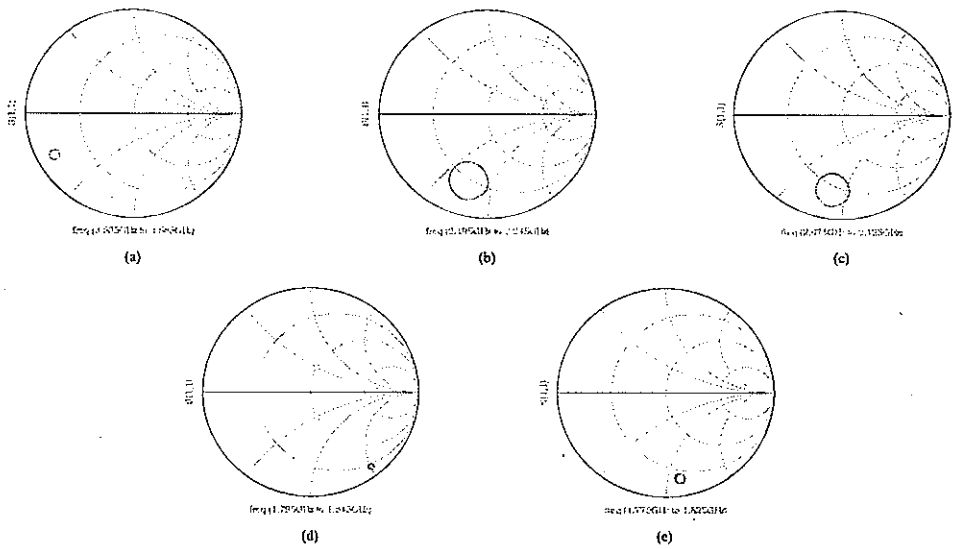

Figure 2.20 Piezoelectric activity of ZnO films deposited at RF power levels of (a) 50 W, (b) 75 W, (c) 100 W, (d) 175 W and (e) 250 W.

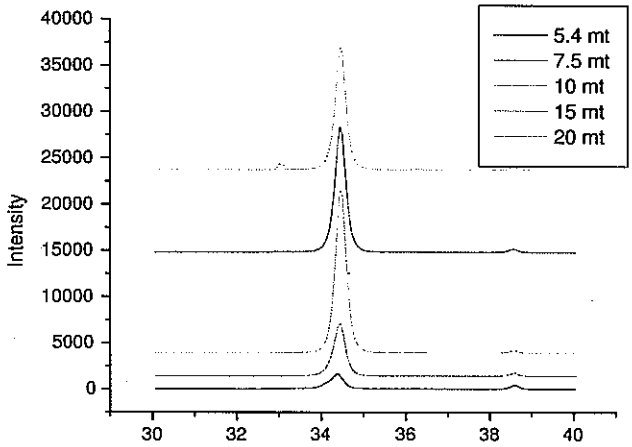

Figure 2.21 XRD scan of ZnO films deposited at different chamber pressures.

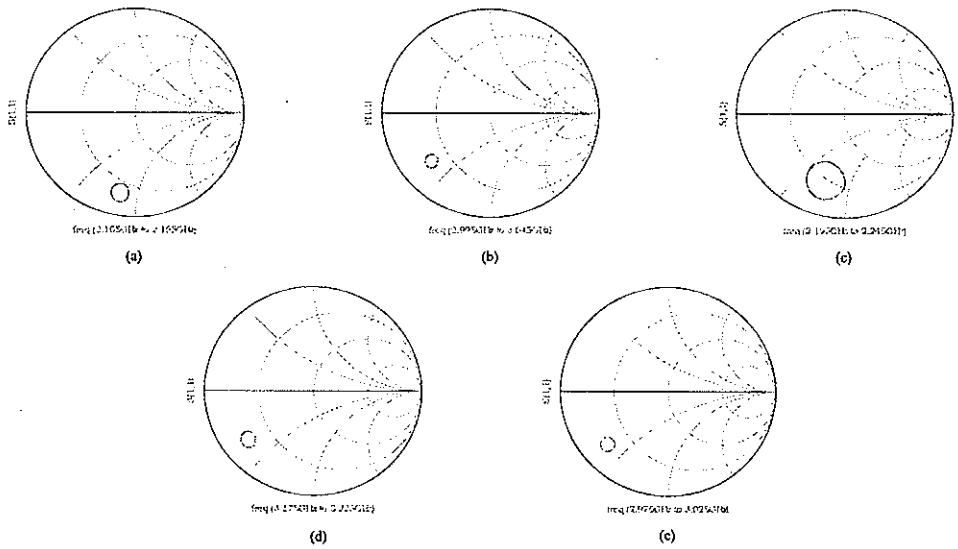

Figure 2.22 Piezoelectric activity of ZnO films deposited at chamber pressures of (a) 5.4 mtorr, (b) 7.5 mtorr, (c) 10 mtorr, (d) 15 mtorr, (e) 20 mtorr.

Deposition Parameter	Value
Sputtering Gas	50% Ar + 50% Oxygen
Substrate Temperature	150 °C
RF Power	75 Watts
Deposition Pressure	10 mtorr

Table 2.7 ZnO deposition parameters that produced the best quality piezoelectric ZnO thin film using a 99.999% ZnO target. The target-to-substrate distance was fixed at 2.54 cm and the deposition rate was approximately 1 μm/hr.

2.3.3.5 Deposition Parameters Conclusion

From the above studies, the deposition parameters that produced the best quality ZnO films were determined for the home-built RF sputter system at the MRC. These parameters are listed in Table 2.7.

2.3.3.6 Annealing

After a wafer of piezo-cantilevers had been fabricated using the parameters listed in Table 2.7 to deposit the ZnO, it became clear that these parameters would not be suitable for cantilever fabrication because the ZnO film contained stress and caused the cantilevers to warp (this is discussed more in Chaper 5). A method to reduce film stress was needed. The first obvious approach was to anneal the sample to try to relax the ZnO film. A few groups (37)-(39) have published results showing the influence of post-deposition annealing on the properties of ZnO films. Both groups tried annealing their samples in vacuum (approximately 10^{-6} torr) for 1-16 hrs over a variety of temperatures and determined that an annealing temperature in the range of 300 °C to 400 °C gave lower stress ZnO and improved the (002) c-axis orientation. They also determined that annealing at higher temperatures (600 °C and above) caused the stress in the film increased and the piezoelectric activity to decrease. Therefore, anneal temperatures of 300 - 400 °C was chosen for this study. We did not have a reliable method for testing the stress in the films, but we performed the annealing study to ensure the quality of the ZnO film did not decrease as a result of annealing. The following sections will examine

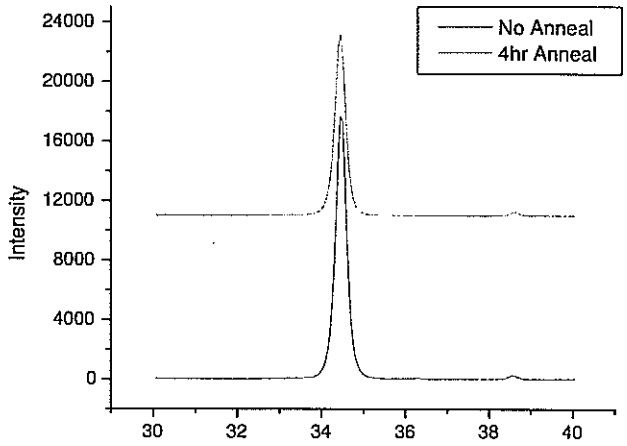

Figure 2.23 XRD results for a ZnO film with no annealing and a ZnO film with a 4 hour anneal at 400 °C.

the quality of the annealed films compared to films that were not annealed. If the quality of the films was comparable, then we know that we could anneal the films during the fabrication process of the piezoelectric cantilevers in hopes of relieving enough stress to give us straight beams.

Since aluminum oxidizes easily, especially at elevated temperatures, the annealing needed to occur in an oxygen-free atmosphere, namely, in vacuum. The most accessible system available for annealing the samples in vacuum was the sputter chamber itself. During annealing, the pressure was in the 10^{-6} range and substrate temperature was 300 °C or 400 °C. An intermediate anneal time of 4 hours was chosen.

Two different anneal tests were performed. In the first experiment two different films of ZnO were deposited with the exact same deposition conditions. One film was not annealed while the other film was annealed at 400 °C for 4 hours in vacuum immediately following the deposition. The XRD results for both films are shown in Figure (2.23).

The resonator structure was then fabricated and the piezoelectricity of both films was

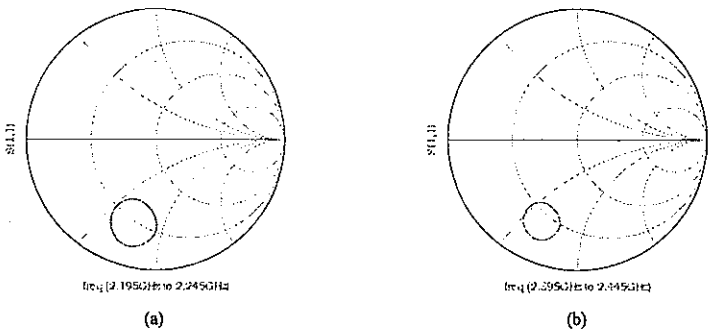

Figure 2.24 Resonator results for a ZnO film with no annealing and a ZnO film with a 4 hour anneal at 400 ^{o}C.

tested. The piezoelectric activity results are shown in Figure 2.24. It is clear from the resonator results that annealing was not detrimental to the piezoelectric activity of the ZnO.

In the second experiment a pre-anneal vs. post-anneal resonator test on one ZnO film was performed. First the ZnO film was deposited, then the resonator structure was fabricated on top of the ZnO film and the piezoelectric activity was tested. After the pre-anneal resonator test, the sample was re-mounted in the sputter system and annealed for 4 hours at 300 ^{o}C. The piezoelectric activity was tested again for the post-anneal test. The results are shown in Figure 2.25.

When the ZnO film was annealed after the top resonator was fabricated (ie. the ZnO film was sandwiched between two aluminum layers) the film turned conductive as is seen in Figure 2.25a. One possible explanation for the increase in conductivity is that the ZnO may break apart into zinc and oxygen where the oxygen is free to move around and react with aluminum to form aluminum oxide. Therefore, the increase in conductivity is most likely due to excess Zn atoms and the absence of oxygen atoms in the ZnO. It was quickly decided that aluminum was not the best choice of metal to use if the samples needed to be annealed.

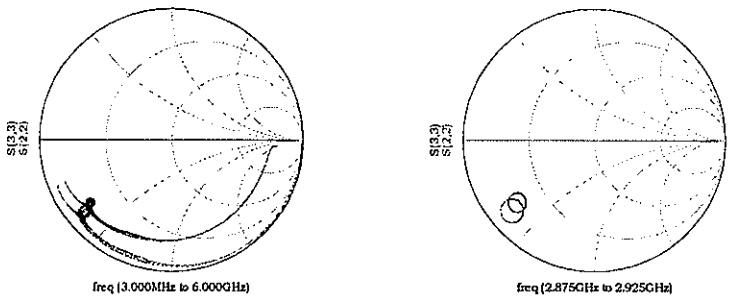

(a) (b)

Figure 2.25 Piezoelectric activity of a resonator before (red) and after (blue) annealing for 4 hours at 300 °C. (a) Resonator response from 3 MHz-6 GHz. Notice the shift of the blue trace toward the center of the Smith Chart indicating that the sample became conductive during the anneal. (b) Resonator response at 2.9 GHz.

2.3.3.7 Gold substrate

Since the presence of aluminum caused the ZnO film to become conductive when annealed, another metal was desired. This metal needed to have a slower oxidation rate than aluminum. Gold was chosen since it does not readily oxidize. Unfortunately, gold is a very poor acoustical material, and therefore, the piezoelectric activity of the resonators could not be directly compared to that of the aluminum resonators. A poor acoustical material tends to have a lot of loss associated with it which decreases the size of the circle on the Smith chart. A resonator fabricated with gold electrodes will have an inherently smaller resonance circle than a resonator fabricated with aluminum electrodes provided the piezoelectric activity of the ZnO film is identical in both cases.

Gold does not adhere very well to surfaces so a very thin layer of titanium or chromium was used as an adhesion layer between the underlying silicon nitride layer and the gold. A Ti/Au layer was used as a bottom electrode since Ti has a hexagonal structure and will promote the growth of ZnO along the (002) direction. The Cr/Au layer was used as a top electrode and patterned into the resonator pattern.

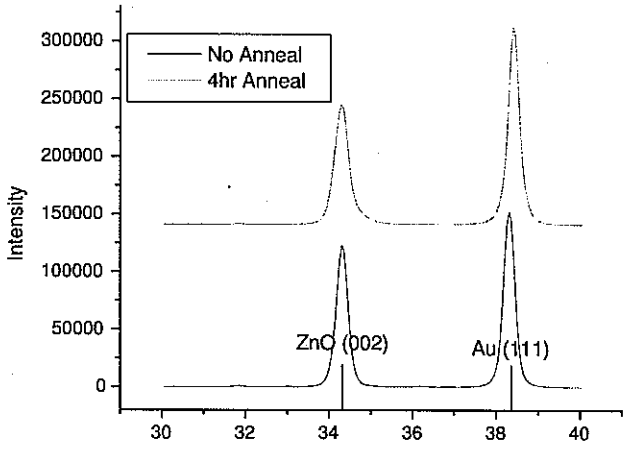

Figure 2.26 XRD scan of two ZnO samples deposited on Ti/Au film; one sample was not annealed, the other sample was annealed for 4 hours at 400 °C.

Two ZnO films with identical deposition parameters were synthesized on top of Ti/Au substrates. One of the films was annealed for 4 hours at 400 °C in vacuum immediately following the deposition. The top metal layer was then deposited and patterned on both of the films to create the resonator structure. Figure 2.26 shows the XRD scan of both the unannealed and the annealed ZnO films. The peak of 2θ=38° is the (111) peak for Au. The (002) peaks of ZnO films grown on gold substrates have much higher intensities than those of the films grown on aluminum, indicating better orientation. Figure 2.27 shows the piezoelectric activity of the ZnO resonators with gold electrodes. The size of the resonance circle is similar to the size of the resonance circle of resonators fabricated with aluminum electrodes. This implies that piezoelectric activity of the resonators fabricated with gold electrodes is higher than that of the resonators with aluminum electrodes. Again we conclude that annealing is not detrimental to the piezoelectric activity of the film.

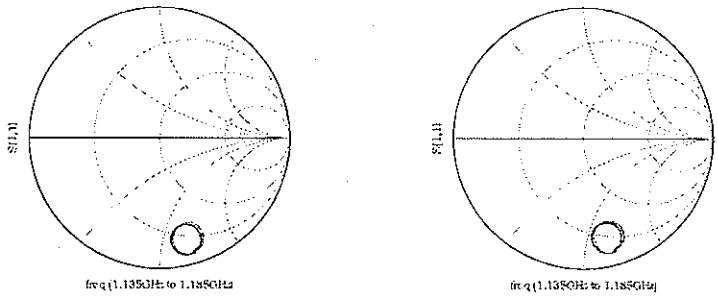

(a) (b)

Figure 2.27 Piezoelectric activity of bulk acoustic wave resonators fabricated on ZnO film deposited on a gold substrate. Figure (a) shows the results with no annealing while (b) shows the results after annealing the ZnO film for 4 hours at 400 °C.

2.3.3.8 SEM images

An SEM image showing the cross section of a ZnO film is shown in Figure 2.28. The deposition parameters of this particular film are those that are listed in Table 2.7. The columnar structure of the film is clearly visible.

2.3.3.9 ZnO Results Summary

The piezoelectric quality of several ZnO films was studied as a function of deposition parameters. Deposition parameters of films giving the best piezoelectric activity are given in Table 2.5. An annealing study was also performed and it was determined that annealing the films did not degrade the piezoelectric activity of the films. However, care is needed when deciding which metal to use if the films need to be annealed. No direct stress measurements were performed, but the amount of stress in the films will be examined later by comparing the straightness of the cantilever beams.

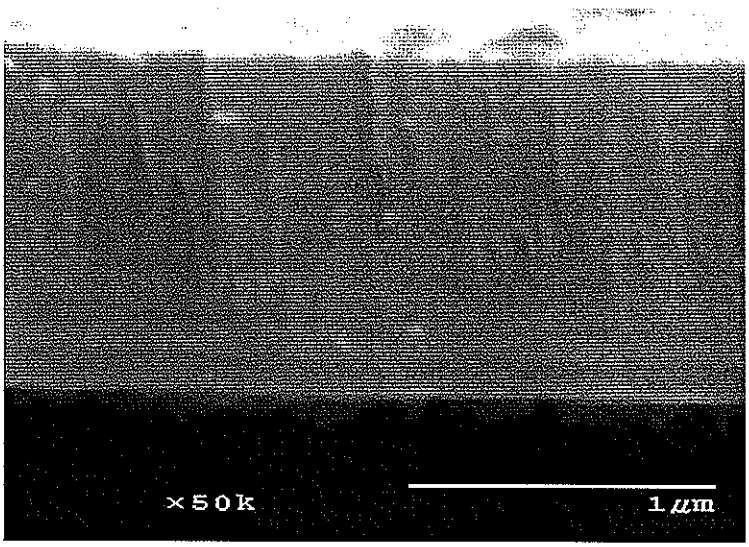

Figure 2.28 SEM image of the cross section of a ZnO film.

CHAPTER 3. Basic Cantilever Design and Fabrication

Before the fabrication of a piezoelectric cantilever could begin, the process steps for a basic cantilever needed to be established. This chapter will first examine design considerations and then the fabrication steps for producing a basic silicon nitride cantilever will be described in detail.

3.1 Mask Design

Designing the mask set for the microcantilevers was a critical step in the fabrication process. Figure 3.1 shows the cross-sectional view of the basic cantilever. The cantilever beam was on the order of 100 μm and far too small to be handled with tweezers, therefore, a larger base was needed so the cantilever could be handled with ease. A bulk silicon base approximately 1600 μm by 3400 μm was designed. The size of the base was designed to fit in a commercial AFM cantilever holder. Silicon nitride was used as the actual beam structure on the front side of the wafer and it was also used as a mask when etching the bulk silicon as KOH does not attack nitride. The reason the cross section of the silicon base is shaped like a trapezoid is because KOH etches silicon anisotropically – the (100) plane etches at a faster rate than the (111) plane.

Several considerations regarding mask design will be outlined in the following sections.

Front-to-Back aligning Because bulk micromachining was used (ie. areas of the bulk silicon would be etched through the entire thickness of the wafer), care was needed to ensure the top and bottom design patterns lined up correctly. If the backside nitride mask was too large, the bulk silicon directly underneath the cantilever would not line up with the front

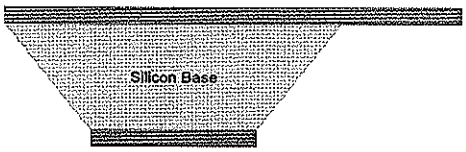

Figure 3.1 Cross sectional view of the proposed basic cantilever structure.

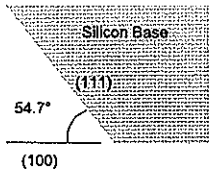

Figure 3.2 Angle between the (111) and (100) planes of a silicon wafer.

design and the beam would not be free standing. If the backside nitride mask was designed too small, the silicon would have etched too much leaving a platform of nitride and making the cantilever more susceptible to breakage. Because the angle between the (111) and the (100) planes is known to be 54.7^o (see Figure 3.2), and because the thickness of the wafer was 425-525 μm, a good estimate of front and back design dimensions was obtained by using simple trigonometery.

Corner design The convex corner created by two perpendicular (111) planes is not protected from KOH etch because, at this particular point, a (411) plane is exposed. The (411) planes etch at a faster rate than not only the (111) planes but also the (100) planes. This results in undercutting of the convex corners (40). Much work has been invested into

researching a design that will protect convex corners from undercutting (40) - (43). Several corner compensation designs have been documented, the one described below was chosen for this project due to its simplicity and because the spatial requirements were not too excessive.

In this project, the biggest concern was to avoid large amounts of undercutting; the quality or sharpness of the corner was not a major concern. The chosen design involved compensation structures added to convex corners in the mask layout. These compensation structures were $< 110 >$ oriented beams extending beyond the corner of the block as seen in Figure 3.3. In this case, the convex corner of the base was protected by a concave corner thus preventing direct undercutting. The end of the compensation beam consisted of two convex corners that would be laterally undercut by the fast etching planes during the etch process. Obviously, the longer the compensation beam, the better protected the convex corner of the base would be from undercutting.

The dimensions of the compensation beam are dependent on the desired etch depth as well as the ratio between the etch rate of the (411) plane to the etch rate of the (100) plane at a specified KOH concentration. The etch rate ratio R(411)/R(100) as a function of KOH concentration can be found in (40) and (42). An approximate ratio is 1.6 for a 30% KOH etch (this KOH concentration was used during the fabrication process). The length of the beam was calculated using the following equation

$$L = 2H(\frac{R(411)}{R(100)}) \tag{3.1}$$

where L is the length of the beam, H is the desired etch depth.

Cantilever dimensions Since the thickness of all the materials was fixed for each wafer, the design parameters of the cantilever beam are length and width. Commercially available cantilevers have beam lengths ranging from 50 μm to 450 μm with widths ranging from 30 μm to 60 μm. The various dimensions depend on the the mode of AFM needed for sampling. Six different cantilever dimensions were used in this project: 100x30 μm, 100x50 μm, 150x30 μm, 150x50 μm, 200x30 μm and 200x50 μm. Figure 3.4 shows a group of five cantilevers that

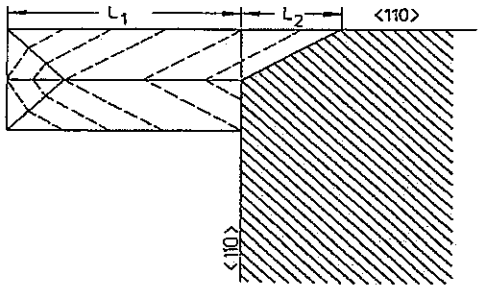

Figure 3.3 Dimensioning of the corner compensation with (110) orientated beams (40).

was part of the mask design for the front side nitride layer (the actual mask contained 124 cantilevers). Figure 4.4 shows the mask design of a group of five cantilevers for the backside nitride layer. Notice the use of the corner compensation design and how the front and back design align with the anisotropic silicon etch step in mind. Also note that the cantilever base was attached to the wafer by small arm structures. After fabrication, the cantilever and base could be easily be removed from the wafer by breaking these arm structures.

3.2 Cantilever Fabrication

Overview Prior to attempting the piezo-cantilever fabrication process, a basic cantilever fabrication process needed to be established. Originally, a cantilever beam made of silicon dioxide was desired mainly because a cantilever made of oxide could be achieved at the Microelectronics Research Center at Iowa State University. Unfortunately, it was soon discovered that a silicon dioxide beam was not sufficient due to the fact that the beams became severely curved thus scattering the laser beam when mounted in the AFM (see Appendix A). As a result, a silicon nitride beam was decided upon.

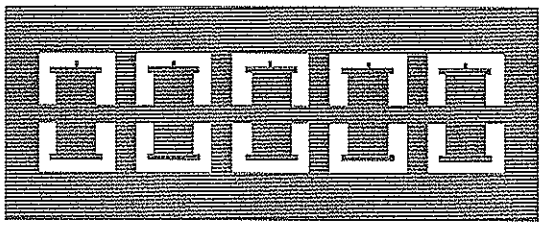

Figure 3.4 Front side design of basic nitride cantilever.

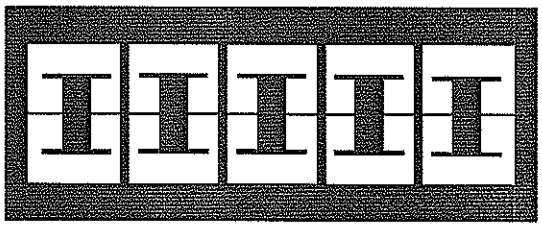

Figure 3.5 Back side mask design of basic nitride cantilever.

Processing at NFC For this process, all fabrication steps were performed at the University of Minnesota Nanofabrication Center. The process began with double sided polished 100 mm (4 inch) diameter n-type (100) silicon wafers of 2-20 Ω-cm resistivity and a thickness of 425-525 μm (Figure 3.6). Next, a 1.7-2.2 μm low-stress low pressure chemical vapor deposition (LPCVD) silicon nitride layer was deposited on both the front and back sides of the wafers (Figure 3.7). The silicon nitride on the front side of the wafer eventually acted as the cantilever beam while the silicon nitride on the back side of the wafer acted as a mask during the silicon etch step. The silicon nitride was deposited in a horizontal LPCVD tube furnace at a pressure of 300 mtorr and temperature of 843 °C. Dichlorosilane was set to flow at 100 sccm and ammonia at 16 sccm. The deposition time was approximately 6 hours to achieve a thickness of $\sim$ 2 μm.

The next step was to pattern the silicon nitride layer on the back side of the wafer using photolithography. (The process of photolithography uses photoresist which is a polymer that changes its structural composition when exposed to UV light. The photolithography process includes coating of the wafers with a photoresist, exposure of the photoresist with an appropriate mask and developing the exposed photoresist to create the desired etch mask for subsequent pattern transfer to the underlying layer. After patterning the photoresist, the underlying layer is then etched using either a wet or a dry etchant.)

The details of the photolithography process used in this project are as follows. To pattern the silicon nitride layer on the back side of the wafer, the wafer was first pre-baked on a hotplate at 115 °C for 60 sec. The pre-bake step drives off water vapor and promotes adhesion of the photoresist to the substrate. Then, the wafer was placed in the hexamethyldisilazane (HMDS) fume tank for 60 sec. The HMDS was used to promote adhesion of the photoresist to the substrate. Next, the wafers were placed on the spinner and a few drops of Microposit 1818 positive photoresist were dropped on the wafer. The wafers were then spun at a speed of 3100 rpm for 30 sec. This particular spin speed for the Microposit 1818 photoresist gave a photoresist thickness of about 1.8 μm (Figure 3.8). The wafers were removed from the spinner and placed on a hotplate at 95 °C for 60 sec for the soft-bake process. The soft-bake

step eliminates solvents from the photoresist, improves adhesion and cures the photoresist to prevent the substrate from sticking to the mask plate during contact exposure.

Next, a Karl Suss MA6/BA6 mask aligner was used to transfer the pattern from the mask plate to the wafer coated with photoresist. With the mask and the wafer in place, the photoresist on the wafer was exposed to ultraviolet light for 6 sec. After the wafer had been exposed, it was dipped in Shipley 351 developer for approximately 20 sec. The developer etched away the exposed areas of the photoresist (Figure 3.9). The wafer was then placed on a hotplate at 120 °C for 60 sec for the hard-bake step. This hard-bake step evaporated any moisture or solvents and hardened the photoresist prior to etching.

After the photoresist was patterned, exposed and developed, the underlying silicon nitride layer was etched (Figure 3.10). The best method for etching silicon nitride is a dry etch which is better known as a Reactive Ion Etch (RIE). RIE uses a plasma to etch the specified areas. The silicon nitride layer was RIE etched using the 320 STS Etcher plasma etching system. The system was set to run a program that etches silicon nitride at approximately 868 $\AA$/min. Therefore, it took slightly over 23 min to etch through a 2 μm silicon nitride layer. (It should be noted that this program etches the Microposit 1818 photoresist at a rate of 736 $\AA$/min. Therefore, a 23 min etch will etch approximately 1.7 μm of photoresist.) This program kept the chamber at a pressure of 100 mtorr with the gasses CF_4 and O_2 at 40 sccm and 4 sccm respectively. The peak to peak voltage was set at 1000 Volts while the bias voltage was 215 Volts.

After the pattern was transferred to the wafer and the silicon nitride layer was completely etched in the designated areas, the remainder of the photoresist was removed using acetone and methanol (Figure 3.11). The wafers were then rinsed in DI water and dried with nitrogen.

The next step was to use a wet KOH etch to etch the silicon (Figure 3.12). KOH etch does not attack silicon nitride at an appreciable rate, therefore, the silicon nitride acts as an excellent mask. The wafers were placed in a heated KOH bath that contained about 30% KOH at a constant temperature of 80 °C. This concentration and temperature produced an etch rate of about 80 μm/hr. Since further processing steps were required, it was not desired to etch

entirely through the wafer as that would make the wafer more vulnerable to breakage or other damage. Therefore, only about 60-75% of the wafer thickness was etched. (The remainder of the wafer would be etched at a later time.) This means that to etch through 75% of a 425-525 μm wafer at 80 μm/hr, the wafer had to be in the KOH bath 4-5 hours.

The next step in the process was to pattern the front silicon nitride layer (Figure 3.13). This pattern produces the dimensions of the cantilever beam. The photolithography steps for patterning and etching the front side silicon nitride layer were exactly the same as the patterning and etching of the backside silicon nitride layer and therefore will not be described in detail.

The photoresist was spun on the front side and the wafer. The MABA6 Karl Suss front-to-back mask aligner was used to align the front side mask with the back side silicon nitride pattern. The wafers were exposed for 6 sec and then placed in the developer for 20 sec. The unwanted areas of silicon nitride were etched away using RIE. And finally, the photoresist was removed using acetone and methanol.

After the front side nitride was patterned and etched, the wafers were again placed in the KOH bath until the wafer was etched entirely through (Figure 3.14). At 30% KOH, this took approximately 1-2 hours. The cantilever beams were then free-standing.

Since silicon nitride is not a good reflecting material, a thin layer of aluminum needed to be deposited on the back side of the cantilever beam (Figure 3.15). Aluminum provides a good reflecting surface for the laser when the cantilever is mounted in the AFM. To deposit aluminum, the wafers were mounted in the Temscal Electron Beam Evaporator at the NFC. Then 1000-2000 $\AA$ of aluminum was evaporated onto the wafer.

The cantilevers were then individually removed from the wafer and tested in the AFM. The results are given in Chapter 5.

Figure 3.6 The process begins with a double sided polished (100) n-type silicon wafer.

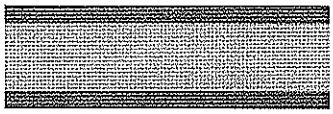

Figure 3.7 A 2 μm thick layer of LPCVD silicon nitride is deposited on both sides of the wafer.

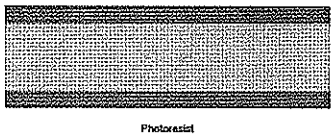

Figure 3.8 The backside of the wafer is coated with photoresist.

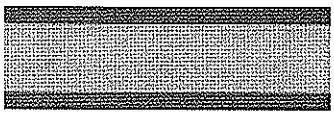

Figure 3.9 Specific areas of photoresist are exposed to UV light and the photoresist is developed.

Figure 3.10 Reactive ion etching (RIE) is used to remove the exposed areas of silicon nitride.

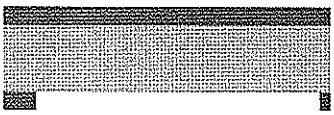

Figure 3.11 The photoresist is then removed using acetone and methanol.

Figure 3.12 The wafers are submerged in 30% KOH solution. KOH etches silicon ansiotropically but does not attack silicon nitride. Only 60% of the wafer is etched to make further processing steps easier.

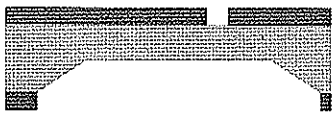

Figure 3.13 The front side of the wafer was photolithographically patterned and the silicon nitride etched using RIE. The front side pattern defines the cantilever structure.

Figure 3.14 The silicon is etched a second time in KOH solution leaving a free standing cantilever beam.

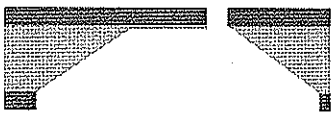

Figure 3.15 A 2000 $\AA$ thick layer of aluminum is evaporated on the back side of the cantilever beam. The aluminum layer provides a good reflecting surface for the laser after the cantilever is mounted in the AFM.

CHAPTER 4. Piezoelectric Cantilever Design and Fabrication

With ZnO films showing good piezoelectricity and with the basic cantilever process mastered, the piezoelectric cantilever fabrication process was attempted. This chapter will describe the piezoelectric cantilever design and then detail the fabrication process used.

4.1 Mask Design

The design considerations for the piezo-cantilever are identical to the design considerations for the basic cantilever with the exception of a few additional particulars which will be described below. Figure 4.1a shows a top down view and Figure 4.1b shows the cross-sectional view of the proposed piezo-cantilever. Silicon nitride was used as the beam material while ZnO was used as the piezoelectric material and aluminum was used as the electrode material for this project.

Electrodes in PiezoCantilever The end product of the piezocantilever requires a sandwich of a bottom electrode, ZnO (the piezoelectric material) and a top electrode all sitting on top of the nitride cantilever beam. The piezoelectric ZnO is excited when an electric field is applied across the thickness of the material, or vice versa, an electrical signal is produced when the beam is strained. Therefore, the mask layout needed to be designed so that both the top and bottom electrodes could be accessed by external means. The top electrode design only required an electrical pad large enough for wire bonding or probes. Access to the bottom electrode was accomplished by designing a square opening in the ZnO layer to allow for electrical contact.

Figure 4.1a shows a top view of the piezoelectric cantilever design. In the design, the actual

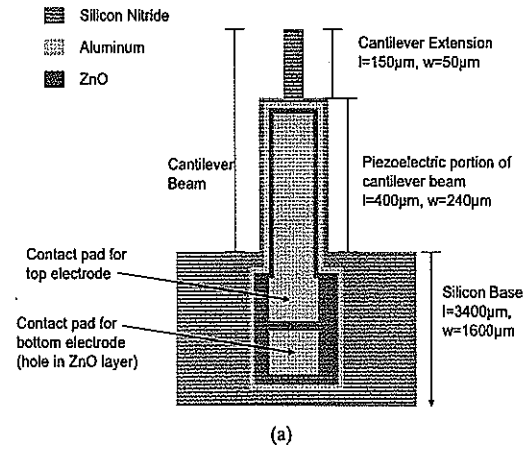

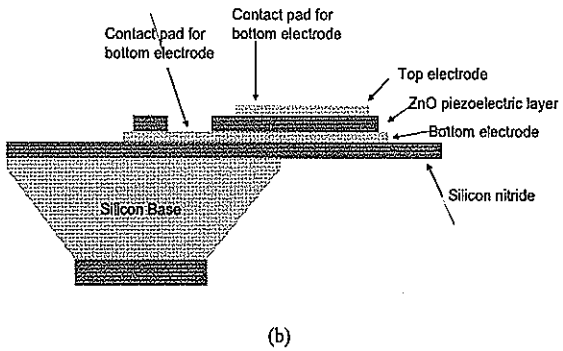

Figure 4.1 The (a) top view and (b) cross sectional view of the piezoelectric cantilever design.

cantilever beam structure consisted of two parts; the first portion contained the ZnO on top of the nitride while the second portion was a cantilever extension that consisted of only silicon nitride. The region with ZnO is the sensor/actuator region and as a result of the addition of extra materials is relatively stiff (44). By designing a cantilever extension, the cantilever is more flexible and versatile for AFM imaging (probing).

Minne *et al.* (44) suggested that the sensitivity of the cantilever can be greatly increased if the majority of the ZnO film is contained on the cantilever beam and not covering large portions of the die or base. Portions of the ZnO film covering the die are insensitive to cantilever vibration. Therefore, these piezocantilever beams were designed with this in mind.

Equipment Considerations The cantilever mask design also depended on what equipment was used in the processing because different pieces of equipment have different substrate size requirements. For example, the first several processing steps were performed at the University of Minnesota Nanofabrication Center. Their equipment is designed for processing 4 inch wafers. Another fabrication step was the deposition of ZnO which was performed at the Microelectronics Research Center at Iowa State University. The RF sputter system used to deposit ZnO allows for substrates no larger than 2 inch in diameter and no smaller than 1.5 inch square. Therefore, the mask needed to be designed to allow for modifications in substrate size.

An easy solution was to plan on cleaving the 4 inch wafer into quarters after the processing in MN was finished. Using sections of one quarter of a 4 inch wafer meant these substrates would be compatible with the RF sputter system substrate holder. Two perpendicular lines were designed in the mask layout that created deep trenches in the silicon after the KOH etch step and facilitated the cleaving of the wafer. The cantilever design was restricted to four small areas on the large wafer. Although this greatly reduces the amount of usable wafer space, it had to be done given the substrate holder variations in the equipment. Figure 4.2 shows the mask design for one quarter section of the 4 inch wafer. The different colors represent the different layers (the different masks for each material).

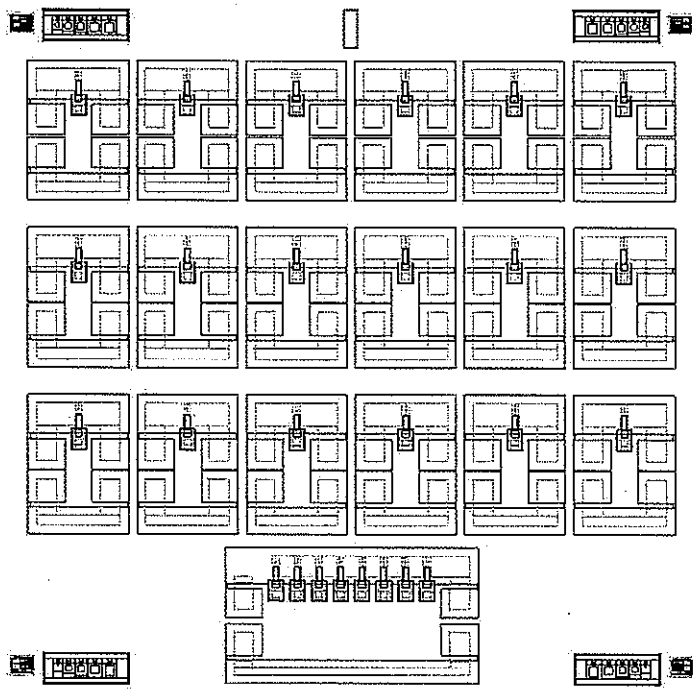

Figure 4.2 Mask layout of the piezoelectric cantilever design. The different colors represent the different layers of the design.

Cantilever dimensions Since the thickness of all the materials was fixed for each wafer, the design parameters of the cantilever are length and width. As was mentioned earlier, the actual cantilever beam consisted of two parts: the first portion of the beam contained the electrodes and piezoelectric layer while the second portion was an extension consisting of only nitride. The portion of the beam consisting of the electrodes and piezoelectric layer had a length and width of 400 μm and 200 μm respectively. The length and width of the cantilever extension was 150 μm and 50 μm respectively.

4.2 Piezo-cantilever Fabrication Steps

Overview The process for piezo-cantilever fabrication utilized both the Nanofabrication Center at the University of Minnesota and the Microelectronics Research Center at Iowa State University. The process began at the University of Minnesota Nanofabrication Center (NFC). The NFC is designed for MEMS and CMOS processing on 4 inch wafers. The facilities at the NFC were used for the deposition of the silicon nitride layer, photolithography and front-to-back side mask aligning, and plasma etching of the front and back side silicon nitride layer. The first KOH etch step was also performed at the NFC. The remainder of the steps were executed at the Microelectronics Research Center at Iowa State University. These steps include the bottom electrode deposition, ZnO deposition and top electrode deposition along with photolithography and etching for each step. The final silicon etch step was also performed at the MRC.

The MRC has CMOS compatible processing designed for 3 inch wafers (or smaller substrates) while the RF sputter system used to deposit ZnO allows for 2 inch square substrates. Therefore, slight modifications needed to be made to the original 4 inch wafers. The masks were designed so that the 4 inch wafers could be cleaved in quarters fairly easily. The smaller sized substrates worked well in the sputter system and for any lithography steps. However, the electron beam evaporator at the MRC was compatible with only 3 inch wafers. In order to overcome this hurdle of mismatched substrate sizes and substrate holders, the substrates were mounted on 3 inch dummy wafers using double sided sticky tape and then mounted in

the evaporator machine. The fabrication process will be described in detail below.

Processing at NFC The process begins at the Univeristy of Minnesota in the Nanofabrication Center. The process steps for the piezocantilever start off identical to the process steps used for the basic cantilever described in Chapter 3 (see Figure 3.6-3.13). The only difference being that the final KOH etch step was not performed until a later time.

Processing at MRC The remainder of the steps were performed at the Microelectronics Research Center at Iowa State University.

After the back silicon nitride etch, silicon etch and front side nitride etch, the next step was to deposit a thin layer of aluminum on the front side of the wafer. This aluminum layer eventually acted as the bottom electrode for the piezoelectric cantilever. The aluminum was deposited using the BJD1800 Themescal Electron Beam Evaporator. Prior to loading the samples into the chamber, the 4 inch wafers were cleaved in quarters (as was designed) and each quarter was mounted onto a 3 inch dummy wafer using double-sided sticky tape. After loading, the chamber was pumped down to a pressure of approximately $5x10^{-7}$ torr. The aluminum was evaporated onto the substrates at a rate of 3 $\AA$/sec until a thickness of 2000 $\AA$ was reached (Figure 4.11). The wafers were unloaded and were then soaked in acetone to remove the double-sided sticky tape.

The next step in the process was to pattern the aluminum layer using photolithography. HMDS was spun on the samples at a rate of 4000 rpm for 40 sec. Then AZ5214-E photoresist was spun on to achieve a photoresist thickness of 1.4 μm. The samples were soft-baked in a 95 ^{o}C oven for 20 min to remove any solvents from the photoresist. The wafers were then removed from the oven and aligned in the MJB3 Karl Suss mask aligner. The wafers were exposed to UV light for 70 sec, then developed using AZ312 MIF Developer (Dilution 1:1:2) for 60 sec. The hard-bake step was then performed by placing the wafers in a 120 ^{o}C oven for 25 min. The first layer of aluminum was etched using the PAN etch recipe (Figure 4.12) (PAN stands for phosphoric acid, acetic acid and nitric acid). This recipe consisted of 40 mL H_3PO_4 (phosphoric acid), 40 mL CH_3COOH (acetic acid), 10 mL HNO_3 (nitric acid), and 10

mL water. 2000 $\AA$ of aluminum was etched in 3 min. Finally, the photoresist was removed using acetone and methanol.

After the bottom aluminum electrode was patterned and etched, the ZnO was deposited (Figure 4.13). A 1 μm thick ZnO film was deposited using an RF magnetron sputtering system. Details of the deposition are described in Section 2.3.1.1. Table 2.7 gives the deposition parameters that were used for the ZnO layer of the piezoelectric cantilevers.

Next, the ZnO layer needed to be patterned and etched using photolithography. This step will be described briefly since it is nearly the same as the MRC photolithography process described previously. Photoresist was applied; the wafer was exposed to UV light through the ZnO mask and then developed in the developer solution. ZnO was etched (Figure 4.14) in an 1:1:30 acetic acid : phosphoric acid : water solution with an etch rate of $\sim$ 5000 $\AA$/min.

After the ZnO was patterned and etched and the photoresist removed, the top electrode layer needed to be deposited and patterned. The preferred method was to use a lift-off process since we do not want to accidently etch the bottom aluminum electrode when performing the top aluminum electrode etch. (In the lift-off process, the photoresist is applied to the wafer, patterned and developed prior to the deposition of the desired material (in our case, aluminum). The metal is then deposited on the entire wafer. The areas where the metal sits on top of the photoresist are then "lifted-off" when the wafer is soaked in acetone.)

The way the mask for the top electrode was designed, a negative photolithography process was required to complete the lift-off rather than the standard positive photolithography as described earlier. The negative photolithography process was very similar to the positive photolithography process with the exception of two additional steps. Photoresist was spun on the wafer (Figure 4.15) and exposed to UV light identical to the positive photolithography process. Next the wafer was placed on a 110 °C hotplate for 90 sec for the reversal bake. Then the wafer was placed back in the mask aligner for a flood exposure of 100 sec (no mask was in the mask aligner at this time). The flood exposure increases the solubility of the unexposed resist and greatly improves developer selectivity and resolution. The wafer was then developed for 60 sec. No hard-bake step was needed – the wafer was ready for metallization.

The wafer was then bonded to a 3 inch dummy wafer using double-sided sticky tape and loaded into the Themescal Electron Beam Evaporator. Approximately 2000 $\AA$ of aluminum was evaporated on the wafers (Figure 4.16). Upon removal from the evaporator, the double-sided sticky tape was removed using acetone. Then the unwanted metal was lifted off by soaking the wafers in an ultrasonic acetone bath for 15-20 min (Figure 4.17).

The next step in the process was to use KOH to etch more silicon. Since KOH attacks to aluminum, the front side of the wafer needed to be protected. A black wax was chosen in this process based on its resistance to KOH. The black wax was dissolved in a small amount of toluene and the liquid was poured over the front of the wafer (Figure 4.18). The wafer was placed on a 50 °C hotplate to evaporate the toluene. The wafer was generally left to sit overnight to ensure all the toluene had evaporated and that the wax had hardened. When the wax was hard, the wafer was submerged in 20% KOH solution at 48 °C. A higher solution temperature was not feasible because the black wax melts at 60 °C. The etch rate of silicon for 20% KOH at 48 °C was 10-16 μm/hr.

It is not recommended to etch completely through the wafer using the KOH solution because once all the silicon etches away, the KOH can seep through tiny capillaries and attack the aluminum on the front side of the wafer. Therefore, the wafer was etched in KOH until approximately 50 μm remained (Figure 4.19).

When approximately 50 μm of silicon remained, the wafers were removed from the KOH and the black wax was removed by soaking the wafer in toluene (Figure 4.20). The remainder of the silicon was etched using the Deep Reactive Ion Etcher (DRIE) at the MRC (Figure 4.21). The DRIE allows for only 4 inch wafers; therefore, the wafer pieces had to be bonded to dummy 4 inch wafers. To bond the two wafers, first photoresist was spun on the 4 inch wafer and then the smaller piece was pressed into the photoresist. The bonded wafers were placed on a 110 °C hotplate for 90 sec before baking them in a 120 °C oven for 25 min to harden the photoresist thus making a stronger bond.

The wafers were then mounted in the Alcatel deep trench reactive ion etching (DRIE) system at the MRC to etch the remainder of the silicon (Figure 4.21). The principle of the

deep trench silicon etching process is an alternating fluorine based etching and passivation of the structures. In this system, the silicon was etched in the presence of SF_6 gas for 7.2 sec and was followed by the passivation step consisting of C_4F_8 gas for 3 sec. The silicon etch rate for the Alcatel system is approximately 6 μm/min. To etch the remaining 50 μm of silicon, an etch time of 8 min was used.

After the wafers had been etched completely through, the bond between the small wafer and the 4 inch dummy wafer had to be removed. This was accomplished by soaking the bonded wafers in acetone for 5-10 min. If needed, the wafers were submerged in an ultrasonic acetone bath to ensure all the photoresist was removed.

The final step in the process was to deposit aluminum on the back side of the cantilever beam (Figure 4.22). The aluminum provides a reflective coating for the laser when the cantilever is mounted in the AFM. The aluminum was deposited using the thermal evaporator at the MRC. Approximately 1000 $\mathring{A}$ of aluminum was deposited. Note: the e-beam evaporator was not used for this step due to a combination of substrate size and warping cantilever beams.

The piezo-cantilevers were then removed individually from the wafer and were ready for testing in the AFM. The results are given in Chapter 5.

Figure 4.3 The process begins with a double sided polished (100) silicon wafer.

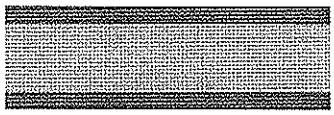

Figure 4.4 A 2 μm thick layer of LPCVD silicon nitride is deposited on both sides of the wafer.

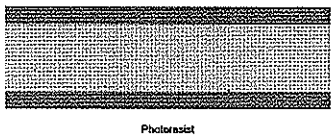

Figure 4.5 The backside of the wafer is coated with photoresist.

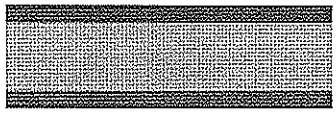

Figure 4.6 Specific areas of photoresist are exposed to UV light and the photoresist is developed.

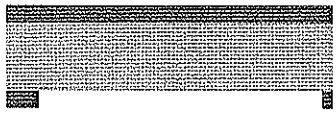

Figure 4.7 Reactive ion etching (RIE) is used to remove the exposed areas of silicon nitride.

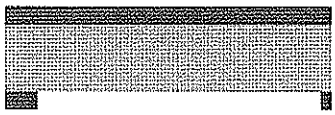

Figure 4.8 The photoresist is then removed using acetone and methanol.

Figure 4.9 The wafers are submerged in 30% KOH solution. KOH etches silicon ansiotropically but does not attack silicon nitride. Only 60% of the wafer is etched to make further processing steps easier.

Figure 4.10 The front side of the wafer was photolithographically patterned and the silicon nitride etched using RIE. The front side pattern defines the cantilever structure.

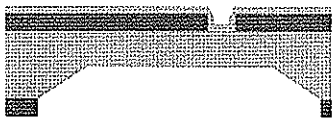

Figure 4.11 2000 $\mathring{A}$ of aluminum is deposited on the front side of the wafer using the electron beam evaporator.

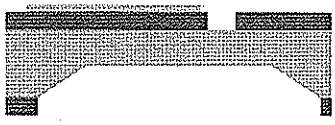

Figure 4.12 The aluminum is photolithographically patterned and the unwanted areas are etched using the PAN etch. This aluminum layer acts as a bottom electrode for the piezo-cantilever.

Figure 4.13 A RF magnetron sputter system is used to deposit piezoelectric ZnO.

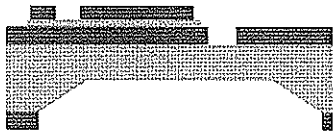

Figure 4.14 The ZnO is photolithographically patterned and the unwanted areas are etched in a weak acid.

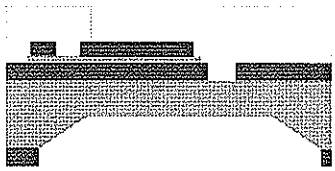

Figure 4.15 The front of the wafer is coated with photoresist and the photoresist is developed. This step is in preparation for lift-off of aluminum.

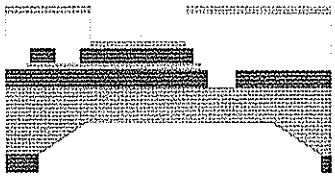

Figure 4.16 2000 $\AA$ of aluminum is evaporated on top of the patterned photoresist.

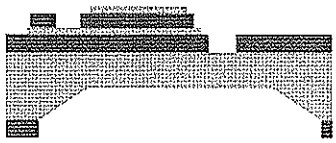

Figure 4.17 The wafer is then soaked in acetone and the unwanted areas of photoresist and aluminum are "lifted off". This aluminum layer acts as a top electrode for the piezo-cantilever.

Figure 4.18 A thick coat of black wax is applied to the front of the wafer. The black wax is resistant to KOH and will protect the metal and ZnO layers from being attacked by KOH.

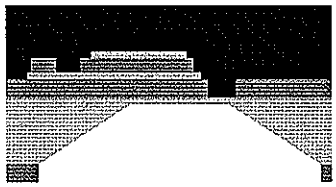

Figure 4.19 The wafer coated with black wax is etched in 20% KOH solution at 48 °C (wax dissolves around 60 °C). The wafer is etched until approximately 50 μm of silicon remain (etching clear through the wafer using KOH will damage the metal and ZnO).

Figure 4.20 The wax is removed by soaking the wafer in toluene.

Figure 4.21 The remaining 50 μm of silicon are etched using the deep reactive ion etcher (DRIE).

Figure 4.22 The final step is to deposit a thin layer of aluminum via thermal evaporation on the backside of the cantilever beam. The thin layer of aluminum serves to make a good reflecting surface for the laser when the cantilever is mounted in the AFM.

CHAPTER 5. Results

Both simple microcantilevers and piezoelectric microcantilevers were successfully fabricated. This chapter will examine the optical photos, SEM images, and any AFM thermal noise measurements obtained as part of this project. Some of the AFM measurements are compared to simulation results using the finite element analysis program ANSYS.

5.1 Basic Cantilever Results

The first step in this project was to fabricate a basic silicon nitride cantilever. The cantilevers were fabricated with two different widths of 30 μm and 50 μm and with three different lengths of 100 μm, 150 μm, and 200 μm.

Optical and SEM photos Optical photos and SEM images of the silicon nitride cantilever are shown in Figure 5.1 and 5.2, respectively. These images are of a cantilever beam with length 150 μm and width 50 μm. Figure 5.2c shows the nitride beam has nearly uniform thickness with just a small amount of undercutting at the beam edges (compare to the silicon dioxide beam in Appendix A).

AFM thermal noise results The thermal noise response (the response of the cantilever beam due to natural vibrations of the surrounding environment) was obtained for the fabricated silicon nitride cantilever beams. Five different beams of equal dimensions were tested to ensure consistency. The averaged values of resonance frequency, mechanical Q and spring constant k are shown in Table 5.1.

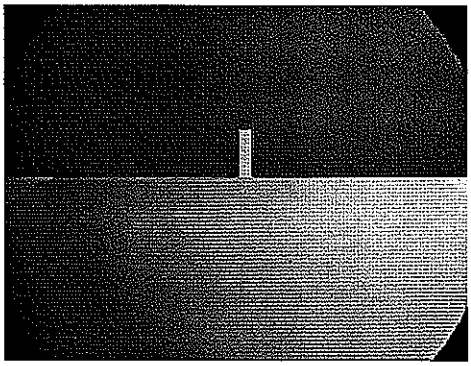

Figure 5.1 Optical photograph of the fabricated silicon nitride cantilever beam.

Beam Dimensions (μm)	Resonant Frequency (kHz)	Mechanical Q	Spring Constant (N/m)
100x30	236.49	239.72	0.59
100x50	236.06	243.1	1.09
150x30	105.07	145.08	0.47
150x50	104.42	139.42	1.053
200x30	60.49	108.54	0.21
200x50	61.82	119.78	0.35

Table 5.1 Resonant frequency, Q, and k obtained from a thermal noise analysis of the fabricated silicon nitride cantilever beams.

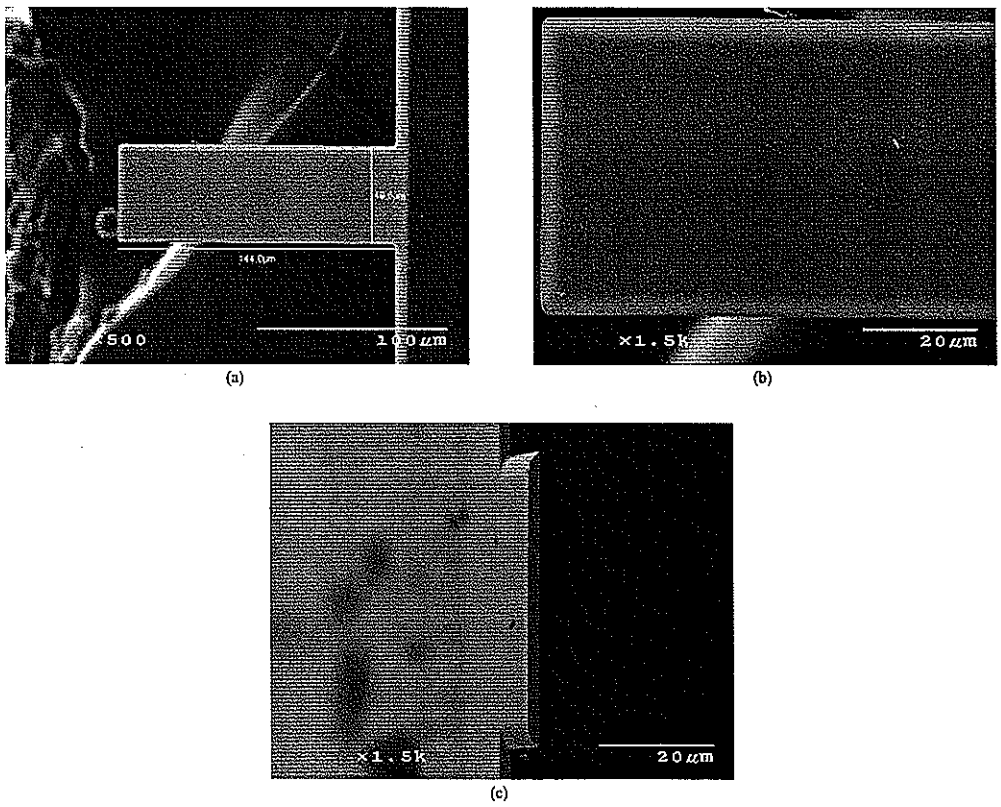

Figure 5.2 SEM images of the fabricated silicon nitride cantilever beam. (a) image of entire beam, (b) close-up image the beam and (c) a near end-on view of the beam showing that the beam is relatively flat.

Beam Dimensions (μm)	Resonant Frequency (kHz)
100x50	305.2
150x50	135.1
200x50	75.8

Table 5.2 Resonant frequency of the silicon nitride beams using the modeling program ANSYS.

ANSYS Finite Element Analysis The finite element modeling program ANSYS was used to model a simple silicon nitride cantilever beam. The 3D model consisted of only the free cantilever beam (not the silicon base) that was fixed at one end by constraining the nodal displacements in the x-, y-, and z-directions. The width of the cantilever was 50 μm while three different lengths of 100 μm, 150 μm and 200 μm were tested. The beam was a silicon nitride beam with a Young's modulus E=260 GPa, Poisson's ratio ν=0.23, and density ρ=3000 kg/m^3. The element type was SOLID45 and the beam was meshed with a rectangular mesh and an element edge length on surface boundaries of 2 μm. No damping was applied to the model. The resonant frequency of the first four harmonics were modeled with the first harmonic results charted in Table 5.2. The resonant frequency of the first harmonic of the modeled cantilever is larger than the resonant frequency of the fabricated beams, but that is to be expected because damping was not included in the model.

5.2 Piezoelectric Cantilever Results

One of the goals in this project was to fabricate piezoelectric microcantilevers. The next section will show optical photos and SEM images of the fabricated cantilevers and talk about why we were not able to test the cantilevers in the AFM. The following section will show simulation results of the modeled cantilever using ANSYS.

Optical and SEM photos An optical photo of the nearly completed cantilever is shown in Figure 5.3. In this photo, the cantilever beam was not free standing as the photo was taken prior to the final silicon etch step. The photo does show that all the layers are aligned and

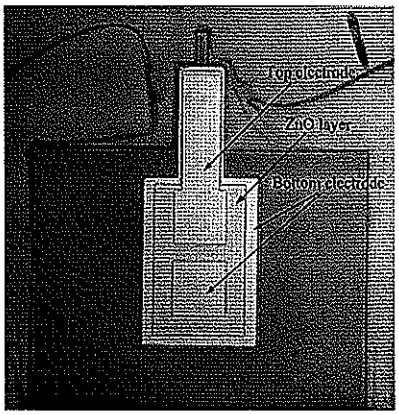

Figure 5.3 Optical photograph of the piezoelectric cantilever beam prior to the final silicon etch step.

there are no shorts existing between the top electrode and the bottom electrode.

The optical photos in Figure 5.4 show two different piezoelectric cantilevers after the silicon was completely etched and the beams were free standing. These beams are warped as is indicated by the dark areas near the end of the beams.

SEM images of the piezoelectric cantilevers were also obtained. A top-down view and a side view of one of the cantilever is shown in Figure 5.5(a) and (b). Notice how the beam is slightly warped. The cantilever in Figure 5.5(c) shows a higher degree of warping that was typical for the other cantilevers on the wafer (the silicon was not completely etched on this particular cantilever beam and can be seen hanging off the side of the cantilever structure). The warping of the beam is not too surprising considering peizoelectric materials are known to have a high amount of intrinsic stress due to the thermal expansion mismatch between the substrate and the piezoelectric thin film (45).

The warping of the cantilevers turned out to be very problematic. In an ideal situation when the cantilever is mounted in the AFM, the laser beam is reflected off the back surface of the cantilever and the reflected signal is then collected in the photodiode. When the cantilever beam is slightly warped, the reflected laser light does not reflect to the photodiode and no signal can be obtained. Therefore, these cantilevers could not be tested in the AFM.

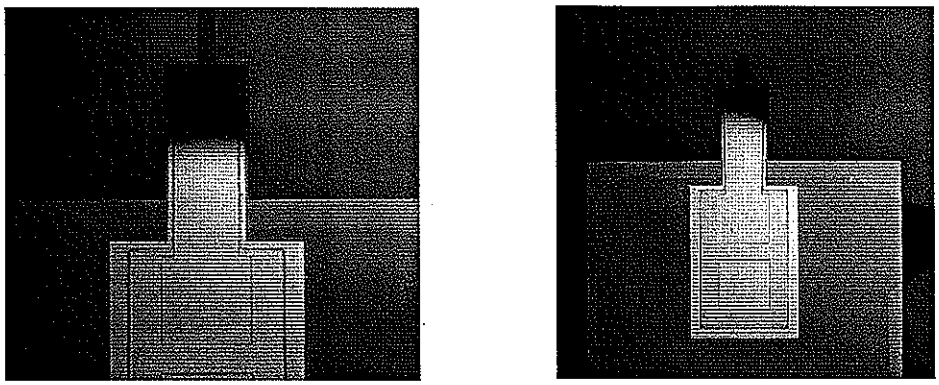

Figure 5.4 Optical photograph of the piezoelectric cantilever beam after the final silicon etch step (a) 10x, (b) 40x. The dark regions near the end of the beam indicate that the beams are warped.

Since the warping was due to stress in the ZnO, a quick fix solution was needed and therefore a short annealing study was performed (see Chapter 2 under the ZnO results section). It was determined that annealing a ZnO film with aluminum electrodes caused the ZnO to become conductive as the zinc and oxygen atoms break apart and the oxygen then bonds with aluminum forming aluminum oxide and leaving vacancies in the film. A material that does not have a tendency to oxidize very quickly was needed and therefore, gold was chosen.

The cantilever fabrication process with gold electrodes was nearly identical to the process with aluminum electrodes with the exception that different etchants were used in the metal etch steps. Since gold is not very good at sticking to other materials, an adhesion layer was needed between the gold and the underlying substrate. For the bottom electrode, a thin layer (200 $\mathring{A}$) of titanium was deposited on the silicon nitride and prior to the 1500 $\mathring{A}$ of gold. The titanium not only acted as an adhesion layer, but it also was used to promote (002) orientated ZnO crystals because titanium has a hexagonal crystal structure similar to ZnO. The adhesion layer for the top electrode was 200 $\mathring{A}$ of chromium.

The idea behind using gold as the metal of choice was because we wanted to anneal the ZnO in an attempt to reduce the stress in the film (in hopes of having straight cantilevers).

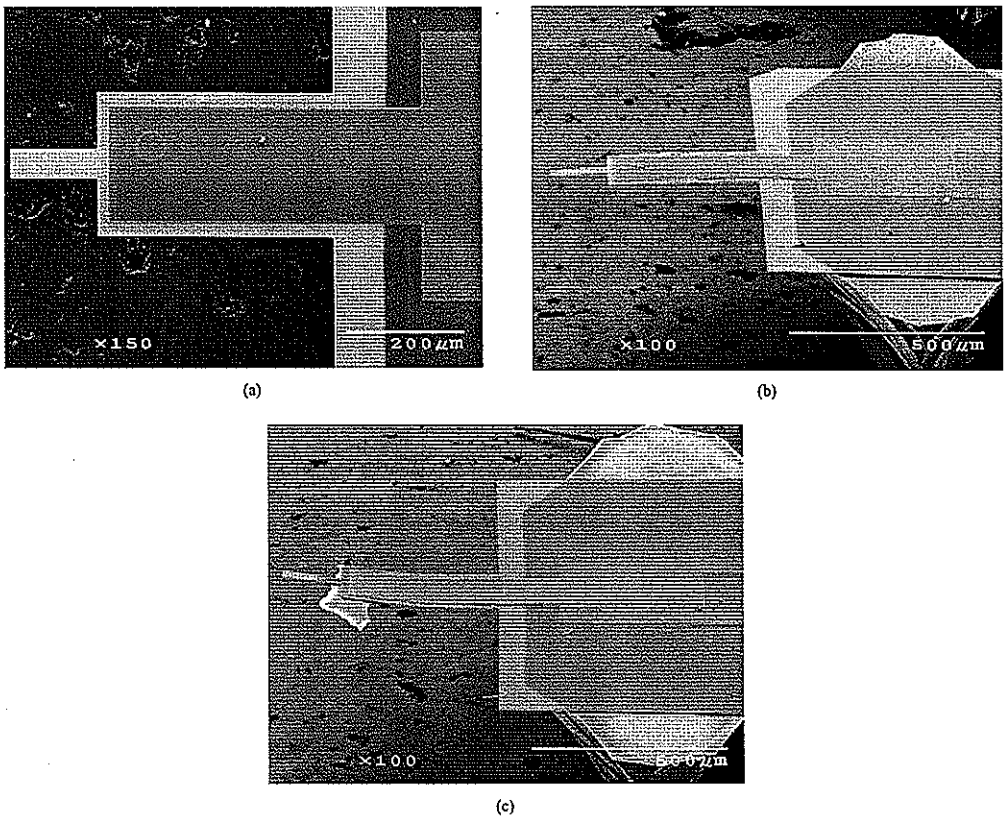

Figure 5.5 SEM images of two fabricated piezoelectric cantilevers. (a) and (b) show the same beam from a top-down view and a side view respectively. (c) shows a different beam with a higher degree of warping that was typical for most cantilevers on the wafer.

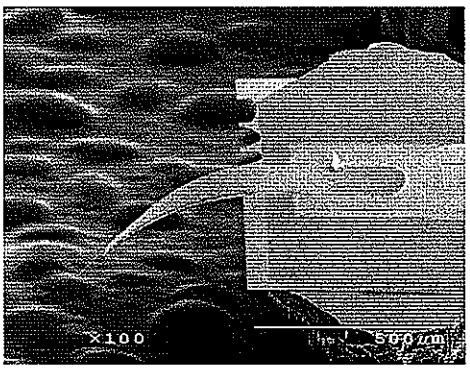

Figure 5.6 SEM image of a piezoelectric cantilever fabricated with gold electrodes.

After the ZnO had been deposited on the cantilevers, the wafers were left in the deposition chamber and annealed at 400 °C for 4 hours in vacuum. When the annealing was complete, the remainder of the fabrication steps were carried out.

Figure 5.6 shows the SEM image of a typical piezoelectric cantilever fabricated with gold electrodes. It is obvious that the cantilevers fabricated with gold electrodes had a significantly higher level of stress than the cantilevers fabricated with aluminum electrodes as can be seen by the different levels of warping that occurred. One explanation for the differences could be because the ZnO film grown on the Ti/Au electrode may have had a higher amount of lattice mismatch thus causing more stress. Or, the stress was due to thermal expansion mismatch between the ZnO and the metal layers. Or, the stress was due to interfacial reactions between the different layers. The twisting of the beam in Figure 5.6 is most likely due to slight variations in ZnO thickness across the beam.

Unfortunately, the idea of annealing the piezoelectric cantilevers fabricated with gold electrodes did not work out. Again, because of the warping, these cantilevers were unusable in the AFM.

As a test to determine if the warping was due to the presence of the metal, one batch of cantilevers were fabricated without the electrodes. These cantilevers were straight, however,

the XRD scan of ZnO on silicon nitride showed the ZnO film was randomly oriented. It is most probable that these cantilevers were not warped because the ZnO film was oriented in a random fashion.

ANSYS Finite Element Analysis The finite element modeling program ANSYS was used to model the piezoelectric cantilever beam. The 3D model consisted of the free cantilever beam including the sensor/actuator region and the extension region but not the silicon base. One end of the beam was fixed constraining the nodal displacements in the x-, y-, and z-directions. The sensor/actuator region consisted of a ZnO on top of silicon nitride. The metal electrodes were omitted from the modeling to simplify the problem. The constants for ZnO ($\epsilon_{\lambda\mu}$, $c_{\lambda\mu}$, and $d_{i\mu}$) are listed in Table 2.4. The constants needed for the silicon nitride material are the same as those used in the basic cantilever analysis (E, ν and ρ). The length and with of the actuator region was 400 μm x 240 μm. The length and width of the beam extension was 150 μm x 50 μm.

Since ZnO is a piezoelectric material a coupled field analysis was required. The element type for the silicon nitride material was SOLID45 while the element type for the ZnO material was SOLID5 (the element type needed for coupled field analysis). The two materials were meshed separately with an element edge length on surface boundaries of 2 μm. No damping was applied to the model.

First, a DC voltage was applied across the piezoelectric ZnO material and the z-displacement at the tip of the beam was determined. Figure 5.7 shows the modeling results of the z-direction displacement when a 5 Volt load is applied across the piezoelectric layer.

The modeled piezoelectric cantilever has an actuator response of 12.5 nm/Volt. Veeco Instrument's commercially available Active Probe has a sensitivity of 20 nm/Volt. Differences between the two values can be attributed to differences in ZnO thicknesses; Veeco's Active Probe has a ZnO thickness of 3.5 μm.

In another modeling experiment, a constant force was applied to the end of the cantilever beam and the voltage response across the piezoelectric layer was determined. In this case, the sensor sensitivity was approximately 0.07 V/μm.

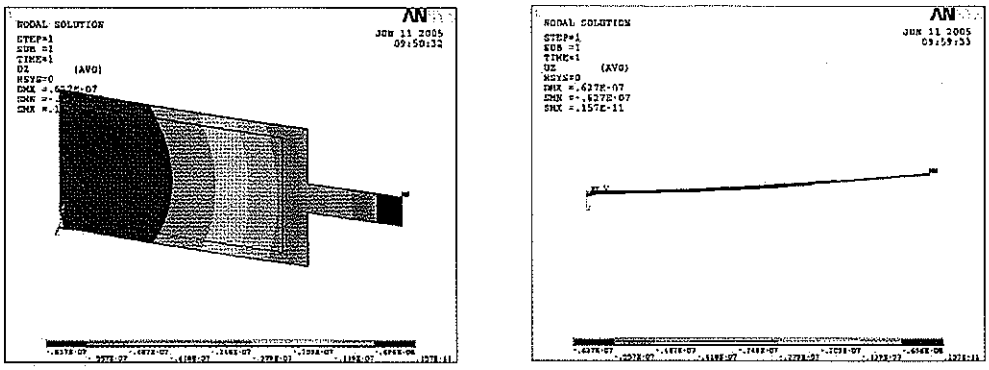

(a) (b)

Figure 5.7 ANSYS modeling results for the piezoelectric cantilever. A DC voltage of 5 Volts was applied across the piezoelectric layer and the resulting z-displacement is shown. The maximum z-displacement was 62.7 nm

A modal analysis was performed to determine the resonant frequency of the beam. The cantilever's first resonance was found to be at 127.8 kHz. Next, a cyclic potential of 3 Volts peak to peak was applied across the piezoelectric layer near the beam's resonant frequency. The z-direction displacement of the tip of the cantilever was recorded and is shown in Figure 5.8. At resonance, the z-direction displacement of the beam is approximately 7.5 μm compared to a 62.7 nm displacement with a 5 Volt DC signal.

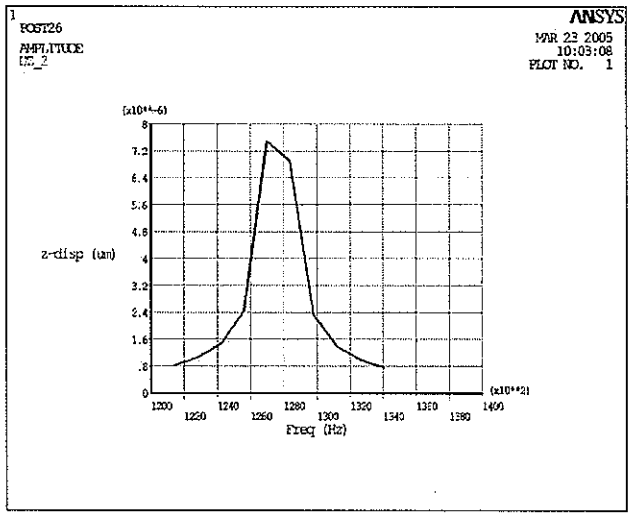

Figure 5.8 A harmonic analysis using ANSYS to model the pieoelectric cantilever. A 3 Volt harmonic signal is applied across the piezoelectric layer and the z-direction displacement at the tip of the beam is shown.

CHAPTER 6. Conclusion

6.1 Summary of Work

The purpose of this research project was to establish a process for the fabrication of MEMS piezoelectric microcantilevers. Before attempting to fabricate the peizoelectric cantilevers, two things were needed. First, a process for bulk micromachining simple cantilevers needed to be developed. This was accomplished and the results were presented. And second, a method for depositing and characterizing good quality piezoelectric zinc oxide films was required. Films grown with various deposition conditions were analyzed and the deposition parameters that produced the highest piezoelectric activity were determined by fabricating bulk acoustic wave resonators and measuring the microwave frequency response. The deposition parameters that produced the highest quality ZnO film were used in the fabrication of the piezoelectric microcantilevers.

A detailed process of the cantilever fabrication was presented and the results were shown. After the cantilevers had been fabricated it was discovered that the ZnO films had a high level of stress and, as a result, the piezoelectric cantilevers were warped and not useful for the AFM. Several annealing studies were performed in an effort to relieve the stress. From these annealing studies, it was decided that aluminum should not be the metal of choice because the ZnO film became conductive as a result of the anneal. It was also discovered that ZnO deposited on gold substrates enhances the quality film orientation as well as increases the piezoelectric activity of the film. However, fabricating the piezoelectric cantilevers with gold electrodes causes the beams to become severely warped even after the film had been annealed.

6.2 Future Work

The piezoelectric cantilevers that were fabricated in this project had one major flaw – they were warped. The warping of the beams can most likely be associated with the intrinsic stress of the piezoelectric ZnO film. One of the first recommendations for future work would be to alleviate the stress in the film. For this to occur, a systematic study is needed to examine the level of stress in the film for different deposition conditions, different annealing times, different annealing temperatures, etc. The best way to measure stress is to measure the curvature of the substrate using a stress analyzer before and after the film deposition. Once the deposition conditions that produce a low stress film while still maintaining good piezoelectric activity have been determined, the piezoelectric microcantilevers can be fabricated using those conditions. Assuming the warping problem is overcome, it is then desired to use the piezoelectric cantilevers in the AFM.

Having established MEMS cantilever processing at Iowa State University, many exciting research areas are possible. One future project could be to fabricate an "on-chip" AFM. The cantilever (presumably a piezocantilever) and all the AFM circuitry could potentially be located on a silicon chip. This would essentially create a portable AFM. Another possible project would be to create an array of cantilevers for increased imaging areas. Much work has been invested into the area of AFM, the possibilities of future work are virtually endless.

APPENDIX A. Oxide Cantilever Fabrication

The original intention of this project was to fabricate cantilevers made of a silicon dioxide beam material. The main reason for this was because silicon dioxide is a regularly deposited material at the Microelectronics Research Center at Iowa State Univeristy and we wanted all fabrication steps to be performed on-site. This chapter will briefly describe the silicon dioxide process steps, show SEM images of the oxide cantilevers and give reasons why the silicon dioxide beam was abandoned.

Oxide Fabrication Process

The process began with double sided polished (100) 3 inch silicon wafers. The wafers were cleaned using the standard clean process at the MRC. Then a 2 μm thick silicon dioxide layer was deposited on both sides of the wafer. The thermal wet oxidation tube was used at a temperature of 1175 °C for approximately 6 hours.

Since the MRC does not have the capabilities for front-to-back side wafer aligning, an additional step was needed before patterning of the cantilever design. In this additional step, a mask consisting of four 1000 μm x 1000 μm squares was used to photolithographically pattern the oxide layer. After the squares were etched into the oxide using buffered hydrofluoric acid (BOE) the wafer was placed in 10% tetramethyl amonium hydroxide (TMAH) solution until the wafer had been etched through its entirety. (TMAH was used because it does not etch oxide as quickly as KOH etches oxide. It was also discovered that KOH left a larger number of pin holes in the wafer.) The idea behind the four squares is that they act as alignment marks for both the front and back side cantilever patterns. The front side cantilever pattern aligns with original square pattern. The back side cantilever pattern aligns with the squares that are

developed after the wafer has been etched through its entirety. Because TMAH etches silicon anisotropically, simple trigonometry can be used to determine the size of the square on the backside.

After the square pattern was etched, both the front and back side of the wafer were photolithographically patterned. Then, the wafer was submerged in BOE solution to etch the oxide pattern on both sides of the wafer. The BOE etch rate is 300 $\AA$/min which translates to an etch time of approximately 1 hour. The photoresist was then removed from both sides of the wafer.

Once the oxide had been etched, the wafer was submerged in 10% TMAH solution until the wafer had been etched through its entirety. The oxide cantilever beams were then free standing.

Oxide Cantilever Results

Optical photos and SEM images of the oxide cantilever beams were obtained. Looking at the SEM images in Figure A.1, it is clear that the cantilever beam is not flat – it does not have uniform thickness. The wedge-shape of the beam is most likely due to the BOE etch step as silicon dioxide etches isotropically in BOE which results in undercutting. In Figure A.1b, the beam is undercut to the point that only a 1 μm wide strip is left untouched. When the beam was mounted in the AFM, most of the reflected laser light scattered off the wedge of the beam and was not collected in the photodiode. The small amount of reflected light that did reach the photodiode was not sufficient enough to produce a good signal. (The cantilever beam typically needs a flat area of at least 20 μm wide to provide a good signal in the photodiode.)

Sine the wedging of the cantilever beam was most likely due to the wet etch of the oxide, a possible next step could have been to try a dry plasma etch to etch the oxide pattern. However, the silicon dioxide cantilever beam fabrication process was abandoned and a silicon nitride beam fabrication process was pursued because silicon nitride is a more robust material which will lead to stronger cantilever beams.

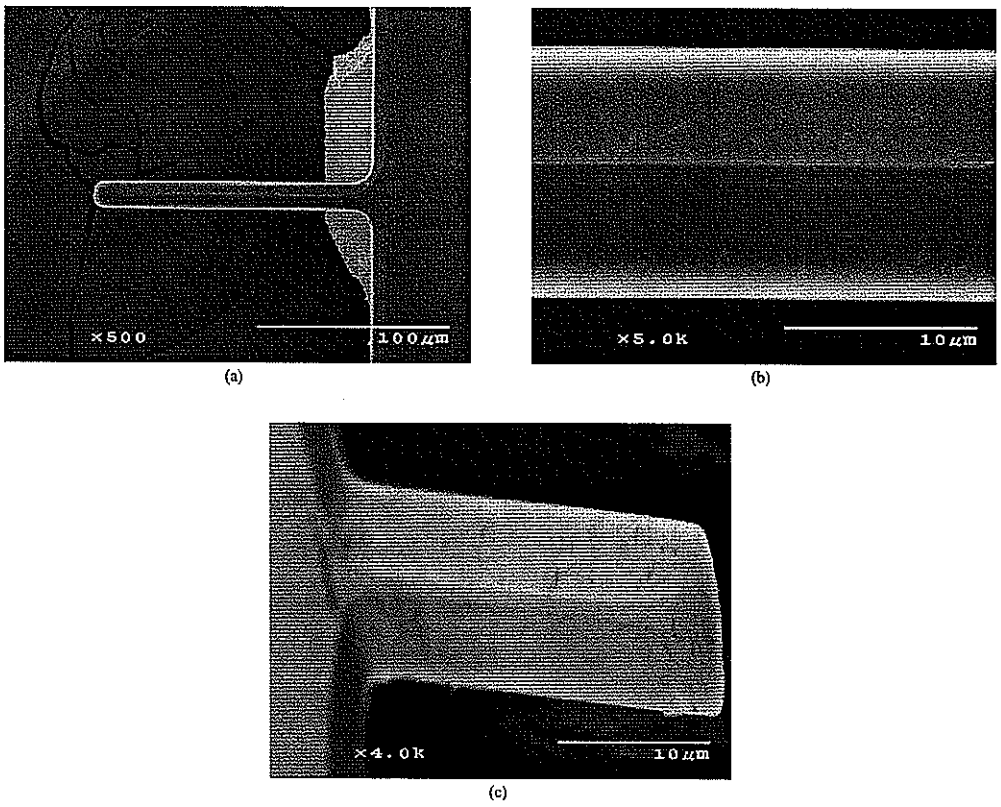

Figure A.1 SEM images of the fabricated silicon dioxide cantilever beam. (a) shows the entire beam, (b) shows a small portion of the beam highlighting the over-etching of the oxide and (c) shows a tilted view of the beam showing the wedged shape.

APPENDIX B. Tip Fabrication

Although the tip is an important feature of the cantilever and the AFM as a whole, the tip was not fabricated as part of this project. In this chapter, the necessary fabrication steps needed to produce tips will be outlined.

Proposed Tip Fabrication Process

Various methods of tip fabrication have been reported depending on the material used for the cantilever and on the desired aspect ratio of the tip. One must also take into consideration any other fabrication steps that may succeed the formation of the tip. All this being said, the following proposed process has the highest success rate for the basic cantilever and the piezoelectric cantilever processes that were described previously in the thesis.

The process begins identically to the basic and piezocantilever processes. A film of LPCVD silicon nitride is deposited on a double sided polished (100) silicon wafer. The silicon nitride will eventually form the beam material.

An 8 μm film of low temperature silicon dioxide (LTO) is then deposited on the entire wafer (Figure B.1). This silicon dioxide layer will eventually form the tip material. Next, a chromium layer is deposited on the front side of the wafer. The chromium layer is used as a mask for the oxide layer as it is resistant to both the plasma and buffered HF wet etch used to form the tip. Before the chromium is patterned and etched, the 8 μm of oxide is etched off the back side of the wafer in wet buffered hydrofluoric acid (HF) (Figure B.2). The chromium layer is then patterned and etched to create a square tip mask (Figure B.3). The size of square that produces the best quality tip (ie. sharp tip with high aspect ratio) needs to be determined experimentally using a test mask prior to fabricating the tip on the cantilever

beam. An approximate size is 5 μm square.

After the chromium layer has been etched and before the photoresist removed, the tip can be formed by first etching the silicon dioxide in a plasma etcher then by using a wet HF etch (Figure B.4). First, approximately 5 μm of LTO should be etched using a RIE plasma etch. The photoresist plus chromium square masks are undercut and the sharp-angle tip defined during this step. After the RIE etching, the remaining LTO film can be etched in buffered HF until the photoresist plus chromium masks are etched free. Again, the etch times should be determined experimentally with a test mask and the quality of the tips should be viewed using the SEM. The ratio of plasma etch time to wet etch time is critical and different ratios should be tested.

After the tips have been fabricated, the remaining process steps can proceed similar to those described in the bulk of the thesis. The main difference being that extra care must be taken to not destroy the tips. This includes a photoresist of at least 8 μm that must be used in all photolithography steps to ensure the oxide tips are not damaged, etched, or get deposited with unwanted material.

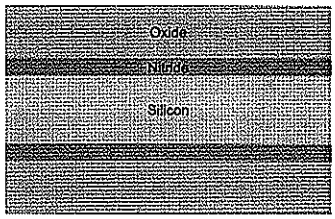

Figure B.1 The tip fabrication process requires an 8 μm thick layer of silicon dioxide deposited on top of the beam material.

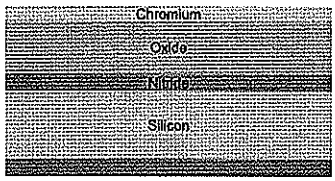

Figure B.2 A chromium film is sputtered on the top oxide layer. The backside oxide layer is completely etched in HF solution.

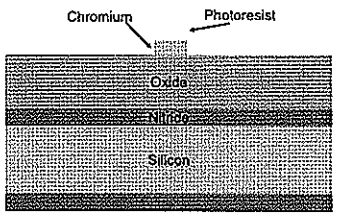

Figure B.3 Next, the chromium layer is photolithographically patterned and etched. The photoresist is not removed.

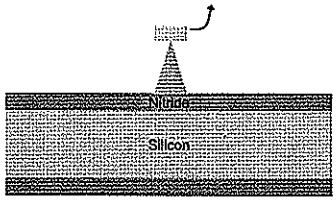

Figure B.4 The oxide is etched first by a plasma RIE etch, then by a wet etch in HF until the chromium/photoresist mask is etched free.

BIBLIOGRAPHY

[1] G. Binning, C.F. Quate, C. Gerber, Atomic Force Microscope, *Physical Review Letters*, **56**, 9, 930, (1986)

[2] www.veecoprobes.com, Data information regarding Veeco Probes commercially available Active Probe, date retrieved 20 July 2005

[3] S.R. Manalis, S.C. Minne, C.F. Quate, Atomic force microscsopy for high speed imagin using cantilever win an integrated actuator and sensor, *Applied Physics Letters*, **68** (5), 871, (1996)

[4] B. Rogers, L. Manning, T. Sulchek, J.D. Adams, Improving tapping mode atomic force microscopy with piezoelectric cantilevers, *Ultramicroscopy*, **100**, 267, (2004)

[5] T. Itoh, T. Suga, Piezoelectric sensor for detecting force gradients in atomic force microscopy, *Japanese Journal of Applied Physics*, **33**, 334, (1994)

[6] S. Watanabe, T. Fuji, Microfabricated piezoelectric cantilever for atomic force microscopy, *Review of Scientific Instruments*, **67** (11), 3898, (1996)

[7] P.F. Indermuhle, G. Schurmann, G.A. Racine, N.F. de Rooij, Fabrication and characterization of cantilevers with integrated sharp tips and piezoelectric elements for actuation and detection for parallel AFM applications, *Sensors and Actuators A*, **60**, 186, (1997)

[8] M.J.Madou, *Fundamentals of Microfabrication*, New York: CRC Press, (1997)

[9] http://ruby.colorado.edu/ smyth/min/zincite.html, University of Colorado Joe Smyth's Mineral Structural Data page, Figure of crystal structure of ZnO, date retrieved: 20 July 2005

[10] T.Ikeda,*Fundamentals of Piezoelectricity*, Oxford University Press, (1990), p.222

[11] J.F. Rosenbaum, *Bulk Acoustic Wave Theory and Devices*, Artech House, (1988), p. 455

[12] S. Chu, W. Water, J. Liaw, Influence of postdeposition annealing on the properties of ZnO films prepared by RF magnetron sputtering. *Journal of the European Ceramic Society*, **23**, 1593, (2003)

[13] M.N. Kamalasanan, S. Chandra, Sol-gel synthesis of ZnO thin films, *Thin Solid Films*, **288**, 112, (1996)

[14] F.D. Paraguay, W.L. Estrada, D.R.N. Acosta, E. Andrade, M. Miki-Yoshida, Growth, structure and optical characterization of high quality ZnO thin films obtained by spray pyrolysis, *Thin Solid Films*, **350**, 192, (1999)

[15] H. Funakubo, N. Mizutani, M. Yonetsu, A. Saiki, K. Shinozaki, Orientation control of ZnO think film prepared by CVD, *Journal of Electroceramics*, **4:S1**, 25, (1999)

[16] K. Sakurai, M. Kanehiro, K. Nakahara, T. Tanabe, S. Fujita, S. Fujita, Effects of oxygen plasma condition on MBE growth of ZnO, *Journal of Crystal Growth*, **209**, 522, (2000)

[17] T. Yamamoto, T. Shiosaki, A. Kawabata, Characterization of ZnO piezoelectric films prepared by RF planar-magnetron sputtering, *Journal of Applied Physics*, **51**(6), 3113, (1980)

[18] J. Molarius, J. Kaitila, T. Pensala, M. Ylimlammi, Piezoelectric ZnO films by RF sputtering, *Journal of Material Science: Materials in Electronics*, **14**, 431, (2003)

[19] R. Ondo-Ndong, G. Ferblantier, F. Pascal-Delannoy, A. Boyer, A. Foucaran, Electrical Properties of zinc oxide sputtered thin films, *Microelectronics Journal*, **34**, 1087, (2003)

[20] J.G.E. Gardeniers, Z.M. Rittersma, G.J. Burger, Preferred orientation and piezoelectricity in sputtered ZnO films, *Journal of Applied Physics*, **83**, No. 12, 7844, (1998)

[21] J.D. Plummer, M.D. Deal, P.B. Griffin, *Silicon VLSI Technology: Fundamentals, Practice and Modeling*, Prentice Hall, (2000), p.539

[22] M.J. Madou, *Fundamentals of Microfabrication*, New York: CRC Press, (1997), p.99

[23] J. Molarius, J. Kaitila, T. Pensala, M. Ylimlammi, Piezoelectric ZnO films by RF sputtering, *Journal of Material Science: Materials in Electronics*, **14**, 431, (2003)

[24] J.G.E. Gardeniers, Z.M. Rittersma, G.J. Burger, Preferred orientation and piezoelectricity in sputtered ZnO films, *Journal of Applied Physics*, **83**, No. 12, 7844, (1998)

[25] A. Cimpoiasu, N.M. van der Pers, Th.H. de Keyser, A. Venema, M.J. Vellekoop, Stress control of piezoelectric ZnO films on silicon substrates, *Smart Material Structures*, **5**, 744, (1996)

[26] S.H. Park, B.C. Seo, G. Yoon, Two-Step deposition process of piezoelectric ZnO film and its application for film bulk acoustic resonators, *Journal of Vacuum Science and Technology A*, **18** (5), 2432, (2000)

[27] D. Schroder, *Semiconductor Material and Device Characterization* - 2nd ed., John Wiley and Sons, Inc., New York, (1998), p.605

[28] P. Yeh, *Optical Waves in Layered Media*, John Wiley and Sons, New York, (1988), p. 280

[29] http://www.mrl.ucsb.edu/mrl/centralfacilities/xray/xray-basics/Xray-basics.html University of California, Santa Barbra, Materials Research Lab Central Facilities, figure of lattice planes and x-rays, date retrieved 20 July 2005

[30] H.F. McMurdie, M. Morris, E. Evans, B. Paretzkim, W. Wong-Ng, and L. Ettinger, JCPDS Card No. 06-1451, *Powder Diffraction*, 1, 76, (1986)

[31] http://www.stanford.edu/class/ee113/handouts/lecturenotes/lecture6-matching.pdf Stanford University Electrical Engineering course EE113, Smith Chart figure, date retreived 15 May 2005

[32] W. Jeong, G. Park, Electrical and optical properties of ZnO thin film as a function of deposition parameters, *Solar Energy Materials and Solar Cells*, **65**, 37, (2001)

[33] S. Park, B. Seo, G. Yoon, Two-step deposition process of pieoelectric ZnO film and its application for film bulk acoustic resonators, *Journal of Vacuum Science and Technology A*, **18**(5), 2432, (2000)

[34] J. Molarius, J. Kaitila, T. Pensala, M. Ylilammi, Piezoelectric ZnO films by R.F. sputtering, *Journal of Materials Science: Materials in Electronics*, **14**, 431, (2003)

[35] R. Ondo-Ndong, G. Ferblantier, F. Pascal-Delannoy, A. Boyer, A. Foucaran, Electrical properties of zinc oxide sputtered thin films, *Microelectronics Journal*, **34**, 1087, (2003)

[36] J.G.E. Gardeniers, Z.M. Rittersma, G.J. Burger, Preferred orientation and piezoelectricity in sputtered ZnO films, *Journal of Applied Physics*, **83** No.12, 7844, (1998)

[37] A. Cimpoiasu, N.M. van der Pers, T.H. de Keyser, A. Venema, M.J. Vellekoop, Stress control of piezoelectric ZnO films on silicon substrates, *Smart Material Structures*, **5**, 744, (1996)

[38] S. Chu, W. Water, J. Liaw, Influence of postdeposition annealing on the properties of ZnO films prepared by RF magnetron sputtering, *Journal of the European Ceramic Society*, **23**, 1593, (2003)

[39] S.S. Lee, R.M. White, Self-excited piezoelectric cantilever oscillators, *Sensors and Actuators A*, **52**, 41, (1996)

[40] P. Enoksson, New Structure for corner compensation in anisotropic KOH etching, *Journal of Micromechanical Microengineering*, **23**, 141, (1997)

[41] H. Sandmaier, H.L. Offereins, K. Kuhl, W. Lang, Corner compensation techniques in anisotropic etching of (100)-silicon using aqueous KOH, *Solid State Sensors and Actuators*, 1991 International Conference on Transducers, 456, (1991)

[42] G.K. Mayer, H.L. Offereins, H. Sandmaier, K. Kuhl, Fabrication of non-underetched convex corners in anisotropic etching of (100)-silicon in aqueous KOH with respect to novel micromechanic elements, *Journal of Electrochemical Society*, **137**, No. 12, 3947, (1990)

[43] M. Shikida, K. Nanbara, T. Koizumi, H. Sasaki, M. Odagaki, K. Sato, M. Anso, S. Furuta, K. Asaumi, A model explaining mask-corner undercut phenomena in anisotropic silicon etching: a saddle point in the etching-rate diagram, *Sensors and Actuators A*, **97-98**, 758, (2002)

[44] S.C. Minne, S.R. Manalis, A. Atalar, C.F. Quate, Contact imaging in the atomic force microscope using a higher order flexural mode combined with a new sensor, *Applied Physics Letters*, **68**, No. 10, 1427, (1996)

[45] T. Itoh, T. Suga, Development of a force sensor for atomic force microscopy using piezoelectric thin films, *Nanotechnology*, **4**, 218, (1993)

Acknowledgements

I would like to thank Dr. Robert Weber and Dr. Murti Salapaka for giving me an opportunity to work on this project. I would also like to thank Dr. David Cann for serving on my committee. I want to thank Dr. Vik Dalal and Dr. Gary Tuttle at the Microelectronics Research Center for allowing me to use their equipment. I also want to thank Max Noack for helping me with the sputter system at the MRC. Part of this project utilized the Nanofabrication Center at the University of Minnesota. The NFC receives support from the National Science Foundation through the National Nanotechnology Infrastructure Network (ECS 0335765).